Chem Soc Rev

REVIEW ARTICLE

View Article Online
View Journal | View Issue

Cite this: *Chem. Soc. Rev.*, 2016, **45**, 3221

Coupling carbon dioxide reduction with water oxidation in nanoscale photocatalytic assemblies

Wooyul Kim,† Beth Anne McClure,‡ Eran Edri and Heinz Frei*

Received 24th January 2016

DOI: 10.1039/c6cs00062b

www.rsc.org/chemsocrev

The reduction of carbon dioxide by water with sunlight in an artificial system offers an opportunity for utilizing non-arable land for generating renewable transportation fuels to replace fossil resources. Because of the very large scale required for the impact on fuel consumption, the scalability of artificial photosystems is of key importance. Closing the photosynthetic cycle of carbon dioxide reduction and water oxidation on the nanoscale addresses major barriers for scalability as well as high efficiency, such as resistance losses inherent to ion transport over macroscale distances, loss of charge and other efficiency degrading processes, or excessive need for the balance of system components, to mention a few. For the conversion of carbon dioxide to six-electron or even more highly reduced liquid fuel products, introduction of a proton conducting, gas impermeable separation membrane is critical. This article reviews recent progress in the development of light absorber–catalyst assemblies for the reduction and oxidation half reactions with focus on well defined polynuclear structures, and on novel approaches for optimizing electron transfer among the molecular or nanoparticulate components. Studies by time-resolved optical and infrared spectroscopy for the understanding of charge transfer processes between the chromophore and the catalyst, and of the mechanism of water oxidation at metal oxide nanocatalysts through direct observation of surface reaction intermediates are discussed. All-inorganic polynuclear units for reducing carbon dioxide by water at the nanoscale are introduced, and progress towards core–shell nanotube assemblies for completing the photosynthetic cycle under membrane separation is described.

Molecular Biophysics and Integrated Bioimaging Division, Lawrence Berkeley National Laboratory, University of California, Berkeley, California 94720, USA. E-mail: hmfrei@lbl.gov

† Current address: Dept. of Chemical and Biological Engineering, Sookmyung Women's University, Yongsan-gu, Seoul 04310, Korea.

‡ Current address: Analytical Services Laboratory, E. & J. Gallo Winery, Modesto, CA 95354, USA.

Wooyul Kim

Wooyul Kim has been a post-doctoral fellow with Dr Heinz Frei at the Lawrence Berkeley National Laboratory since 2013. He received his PhD from POSTECH under the direction of Professor Wonyong Choi in 2012, and his bachelor's degree from Kwangwoon University in 2006. During his PhD period, he joined Osaka University (Professor Tetsuro Majima) as a visiting researcher in 2009, 2010, and 2012. He started his independent career at Sookmyung Women's University as an Assistant Professor in the Department of Chemical and Biological Engineering in March 2016. His research effort focuses on photocatalysis for solar energy conversion and environmental applications.

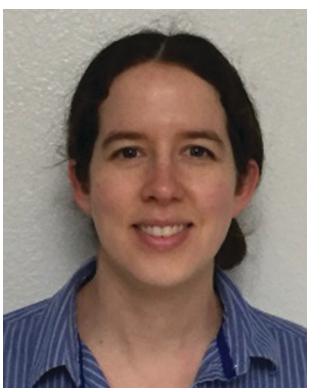

Beth Anne McClure

Beth Anne McClure is currently a Senior Chemist in the Analytical Services Laboratory of E. & J. Gallo Winery. She completed her PhD at Ohio University under the supervision of Prof. Jeffrey Rack, with research focused on the kinetics and spectroscopy of photochromic ruthenium sulfoxide complexes. Beth completed post-doctoral studies in the lab of Dr Heinz Frei, working on the kinetics of metal-to-metal charge transfer in all inorganic oxo-bridged metal compounds.

1. Introduction

Conversion of carbon dioxide and water with sunlight in a single integrated system, which is the goal of artificial photosynthesis, enables the utilization of non-arable land for generating a renewable transportation fuel. Single integrated systems are attractive from the standpoint of minimizing the balance of system components, which is essential for very large scale use. A challenging requirement is that all components from light absorber to catalyst to separation membrane operate efficiently under one and the same, preferably benign, environmental conditions. Harsh conditions, especially regarding pH, are likely to limit the durability of components, while benign environments open up a broader range of materials to choose from, in particular earth abundant materials. Yet existing membrane materials require either strong acid or base for working properly.[1,2] Here, Nature's design of closing the photosynthetic redox cycle of oxidizing water and generating the initial stable reduction intermediates on the nanoscale provides inspiration for an artificial photosystem that avoids extreme conditions or the need for additional reagents to maintain efficient performance in a mild environment. Completing redox cycles on the shortest possible length scale – the nanometer scale – minimizes major side reactions and efficiency degrading processes, in particular large resistance (ohmic) losses caused by charge transport over macroscale distances in mild pH environments. Artificial photosystems that close redox cycles on the nanoscale have emerged only very recently. Inclusion of a proton conducting membrane in such a system will be critical for preventing cross and back reactions, especially when coupling H_2O oxidation with CO_2 conversion to form highly reduced products. An equally important challenge in developing artificial solar fuel systems is the use of robust component materials, which at the same time allows for tuning of their electronic properties. Fine tuning of electronic properties is required for the precise redox matching of the components of the assembly in order to convert a maximum fraction of the solar photon energy to chemical energy while maintaining sufficient catalytic rates for keeping up with the photon flux at maximum solar intensity.

In order to address these requirements, we have pursued an approach that uses as light absorbers all-inorganic molecular units in the form of oxo-bridged heterobinuclear groups covalently anchored on an insulating solid oxide such as silica. The metal-to-metal charge transfer transitions (MMCTs) of these units exhibit absorption deep into the visible region and allow us to combine robustness with the electronic tunability of a molecularly defined chromophore. Based on this approach, and by introducing a photodeposition method for the spatially directed assembly of metal oxide nanocatalysts, it recently became possible to close the cycle of carbon dioxide reduction by water on the nanoscale. While this is a useful step for advancing complete photosynthetic cycles in an artificial system, a critical ingredient not yet present in such a system is a proton conducting membrane for separating the incompatible oxidation and reduction chemistries, thus avoiding back and cross reactions. Towards this end, we are developing nanoscale assemblies in the form of Co oxide–silica core–shell nanotubes with molecular wires embedded in the silica shell that separate the water oxidation catalysis on the inside from the light absorber and carbon dioxide reduction chemistry on the outside of the tube. Macroscale arrays of such nanotubes would constitute a system that completes the redox cycle on the nanoscale while achieving product separation on all length scales. A critical enabling factor for developing such systems is the manipulation of inorganic matter on the nanoscale.

In this review article, we will describe progress towards CO_2 reduction by H_2O, which means the coupling of all-inorganic light absorber–catalyst subsystems for CO_2 reduction

$$CO_2 + 2e^- \rightarrow CO + 1/2O_2$$

with subsystems for H_2O oxidation

$$H_2O + 2h^+ \rightarrow 1/2O_2 + 2H^+$$

Eran Edri

Eran Edri is currently a postdoctoral fellow at the Lawrence Berkeley National Laboratory (LBNL). He completed his PhD at the Weizmann Institute of Science in Israel (2014) under the guidance of Prof. Gary Hodes where he studied materials for photovoltaic devices. In 2014, after winning a career development award from the Faculty of Engineering Sciences at Ben-Gurion University, Israel, he moved to LBNL to research new ways for closing the artificial photosynthetic cycle on the nanometer scale. His research interests are photo-electronic processes in organic–inorganic materials and their potential uses.

Heinz Frei

Heinz Frei received his Dr.Sc. in Physical Chemistry from the Swiss Federal Institute of Technology (ETH Zuerich, 1977). He was a postdoctoral fellow in the UC Berkeley Chemistry Department (1978–1980). His current research focuses on the synthetic, spectroscopic and mechanistic challenges of the conversion of carbon dioxide and water to a liquid fuel by artificial photosynthesis. A Senior Scientist at the Lawrence Berkeley National Laboratory, he is a recipient of the Werner Prize of the Swiss Chemical Society (1990) and is a Fellow of the American Association for the Advancement of Science (2014).

that affords closing of the complete photosynthetic cycle on the nanoscale. The ultimate goal is the reduction of CO_2 beyond CO to liquid products such as CH_3OH or even CC-bond containing fuels. The work is discussed in the broader context of recent progress in the field of molecular light absorber–catalyst subsystems and the development of complete photocatalytic cycles based on them. The crucial role of nanostructured metal oxides in developing Earth abundant catalysts for water oxidation is discussed and details of the water oxidation mechanism based on dynamic infrared spectroscopy under photocatalytic conditions are described. The challenge in improving the efficiency and scalability of photosystems by separating the half reactions by a proton conducting nanoscale membrane is addressed by the introduction of ultrathin dense phase silica layers with embedded molecular wires. The novel Co oxide–silica core–shell nanotubes serve as a starting point for the development of nanostructured assemblies in the form of macroscale arrays for efficient CO_2 reduction by H_2O under product separation by a membrane.

2. An all-inorganic binuclear light absorber coupled to a CO_2 reduction catalyst

Oxo-bridged heterobinuclear units like $TiOMn^{II}$ or $ZrOCo^{II}$ anchored covalently on silica surfaces shown in Fig. 1–3 possess

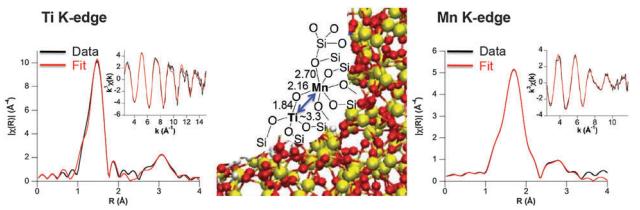

Fig. 1 Structure of the TiOMn heterobinuclear light absorber by EXAFS analysis. Fit of Ti K-edge (left panel) and Mn K-edge EXAFS (right panel) for $TiOMn^{II}$ units anchored in SBA-15 silica pores. The insets show the K-edge fits in *k*-space. Reproduced from ref. 8 with permission from the American Chemical Society.

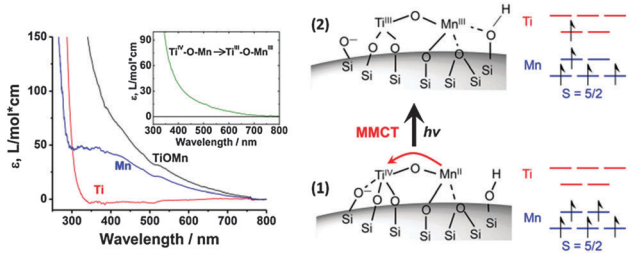

Fig. 2 Optical transmission spectra of the binuclear oxo-bridged TiOMn unit anchored on silica nanoparticles (12 nm) (black trace). Monometallic Ti–SiO_2 (red) and Mn–SiO_2 (blue) samples are shown for comparison. The inset shows the MMCT absorption calculated as the difference of the spectra of the TiMn sample and the Ti and Mn only samples. Cartoon illustrating the MMCT transition from the $Ti^{IV}OMn^{II}$ ground state (1) to the $Ti^{III}OMn^{III}$ excited state (2) and orbital occupancy for high spin configuration. Adapted from ref. 18 with permission from the American Chemical Society.

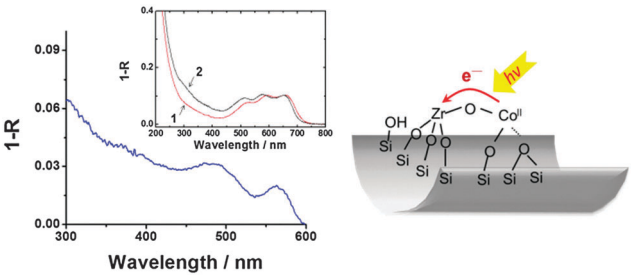

Fig. 3 Diffuse reflectance optical absorption of $Zr^{IV}OCo^{II} \rightarrow Zr^{III}OCo^{III}$ metal-to-metal charge-transfer transition. The trace is the difference of the ZrCo–SBA-15 sample and the monometallic Co^{II}–SBA-15 material. The wave-like behavior in the 500–600 nm region is due to a frequency shift of the Co^{II} spin orbit components to higher energy upon formation of an oxo bridge to Zr as shown in the inset: trace 2, ZrCo–SBA-15; trace 1, Co–SBA-15. The cartoon depicts the binuclear unit on the SBA-15 nanopore surface. Adapted from ref. 7 with permission from the American Chemical Society.

a continuous optical absorption extending from the UV deep into the visible region. Absorption of a photon results in the transfer of an electron from the highest occupied orbital of the donor (*e.g.* Mn or Co) to the lowest unoccupied orbital of the acceptor center (*e.g.* Ti or Zr). The origin of the metal-to-metal charge transfer transition *e.g.*

$$Ti^{IV}–O–Co^{II} \rightarrow Ti^{III}–O–Co^{III}$$

is the sigma bonding overlap of the d orbitals of the Ti and Co centers. Importantly, the excitation process itself results in the separation of charges, a step that is essential for driving oxidation and reduction catalysis with the energy of the absorbed photon.

2.1 Synthesis and spectroscopic characterization of binuclear light absorber units

First demonstrated for $TiOCu^{I}$ and $ZrOCu^{I}$ units,[3,4] solution reactions under very mild conditions using metal precursors with weakly bound ligands allowed us, and subsequently the Hashimoto group, to assemble over a dozen heterobinuclear units on silica surfaces with good selectivity. Concave surfaces of mesoporous silica such as SBA-15 or MCM-41 as well as the convex surface of silica nanoparticles are suitable supports. Donor centers represent most of the upper row transition metals as well as some group B metals, while acceptors are the d^0 elements, Ti or Zr.[3–16] The flexibility in the choice of the donor metal provides a means of matching the redox potential of the light absorber with that of the multi-electron catalyst. In our most recent example, $ZrOCo^{II}$ units were assembled on the nanopore surface of mesoporous silica SBA-15 (1-dimensional system of 8 nm channels separated by 2 nm walls[5]) by anchoring tripodal Zr–OH groups using an established method[6] followed by the exposure of the resulting powder of Zr–SBA-15 particles to $Co^{II}(NCCH_3)_2Cl_2$ in acetonitrile at room temperature. Due to the higher reactivity of the more acidic Zr–OH groups compared to the much more abundant Si–OH groups on the silica nanopore

surface, the Co complex preferentially reacts with ZrOH, resulting in binuclear ZrOCo^{II} units (Zr : Co = 1 : 1, Zr : Si approx. 1 : 100).[7]

Characterization of the geometrical and electronic structure combined with knowledge of the excited state electron transfer properties provides critical information for utilizing the binuclear units as MMCT light absorbers to drive catalysts for CO_2 reduction and H_2O oxidation. Specifically, curve fitting analysis of Extended X-ray Absorption Fine Structure (EXAFS) spectra of K-edges of ZrOCo^{II} and TiOMn^{II} units revealed important insights into the geometrical structure of such systems. For TiOMn^{II} anchored on SBA-15 silica nanopore surfaces, an oxo bridge holds the Ti and Mn centers at a distance of 3.3 Å, from which a TiOMn angle of 111° was derived.[8] The Ti–Mn distance was found to be identical for fits of K-edge EXAFS measurements of Ti and Mn (Fig. 1). Comparison of the EXAFS results for the Ti and Mn centers of the binuclear unit with those for the isolated Ti or Mn centers on the silica surface of monometallic Zr–SBA-15 and Mn–SBA-15 showed that the structure of the first coordination sphere does not change appreciably upon binuclear site formation. The Ti remains tetrahedrally coordinated with a Ti–O distance that varies by just 0.01 Å between isolated and binuclear units. Mn has distorted octahedral geometry both in isolated form and when part of a TiOMn unit.[8] Coordination geometries derived from K-edge curve fitting were confirmed by the characteristic L-edge spectra of tetrahedral Ti^{IV} with an additional coordinated water molecule, and of octahedral Mn^{II}.[9] Similar observations were made for ZrOCo^{II} units, for which the ZrCo distance was found to be 3.4 Å and a ZrOCo angle of 114° was inferred, with good agreement between second shell fitting results for Zr and Co K-edge measurements.[7] The majority (80 percent) of Co centers are part of ZrOCo units with the remainder anchored as isolated centers, indicating high selectivity of the mild synthesis procedure for assembling the binuclear units. Here, too, the Co^{II} center showed the same tetrahedral coordination when anchored as an isolated center in monometallic Co–SBA-15 or part of a binuclear ZrOCo^{II} (or TiOCo^{II}) group, with the Co–O distance essentially unchanged. The finding that metal centers on silica surfaces closely preserve coordination geometries when part of heterobinuclear units suggests that these MMCT units form naturally and do not constitute strained structures. This may explain why a variety of different units can be prepared on silica nanoparticle surfaces by mild synthetic methods.[3,4,7–18]

The onset of MMCT optical absorption lies typically in the green–red spectral region (500–700 nm) and depends on the nature and the oxidation state of acceptor and donor metals. For the TiOMn^{II} and ZrOCo^{II} systems, the spectra shown in Fig. 2 and 3 indicate onsets at around 650 and 550 nm, respectively. While the relative order of the absorption onsets is as one anticipates based on ionization potentials and electron affinities of donors Mn^{II} and Co^{II}, and acceptors Ti and Zr, respectively,[19] the small separation of 100 nm (8 kcal mol^{-1}) for ZrOCo^{II} and TiOMn^{II} seems surprising.[7,10,11] However, because the extinction coefficient of MMCT transitions is determined by the sigma bonding overlap of the d orbitals of the oxo-bridged metals,[20] the only modestly higher onset energy for the ZrOCo^{II} unit compared to the TiOCo^{II} unit can be rationalized by the larger size of the Zr 4d orbitals compared to the Ti 3d orbitals. In addition to revealing the MMCT transition, the green-red range of the spectrum confirms the tetrahedral, high spin structure of Co^{II} by the spin orbit triplet of the Co $^4A_2(F) \rightarrow {}^4T_1(P)$ ligand field transition, which was further corroborated by a characteristic EPR signal.[7,10]

Among other known metal-to-metal charge-transfer systems most closely related to heterobinuclear charge transfer units on silica surfaces are solid mixed oxides investigated in the field of mineralogy.[19–26] For example, minerals featuring edge sharing Ti$^{IV}O_6$ and Fe$^{II}O_6$ octahedra possess MMCT transitions with maxima in the 400–900 nm range and Fe–Ti bond distances in the range of 2.7–3.6 Å, *e.g.* 3.2 Å for the TiFe mixed oxide humite mineral.[24–26] For these mixed oxides, observed MMCT extinction coefficients are similar to those of heterobinuclear groups on silica, which reflects the common electronic origin of the transition and the similar geometry. Among heterobinuclear organometallic complexes, a μ-oxo bridged TiOCr^{III} system[27] features a Ti–Cr separation of 3.13 Å and optical absorption parameters similar to the TiOCr^{III} group on the mesoporous silica surface.[10] Of a series of five heterobimetallic O-bridged complexes featuring a V^{IV} donor and Mn^{II}, Fe^{II}, Co^{II}, Ni^{II}, and Cu^{II} acceptor centers reported recently, the Fe system exhibits an optical V^{IV}OFe^{II} → V^{V}OFe^{I} MMCT absorption centered at 502 nm with an extinction coefficient of 1700 M^{-1} cm^{-1} (Fig. 4A).[28] This spectral assignment is confirmed by the association of the optical transition with a vibrational mode of the oxide bridge observed in resonance Raman measurements. Because all five metal acceptor centers are high spin except for Fe^{II}, only the V^{IV}OFe^{II} MMCT transition is spin allowed and therefore

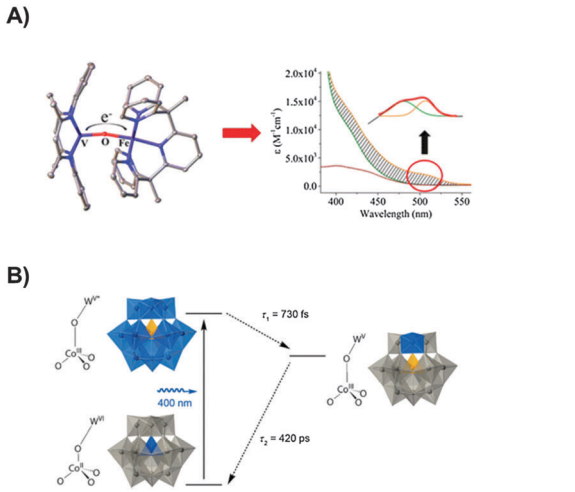

Fig. 4 Metal-to-metal charge-transfer absorptions of oxo-bridged heterobimetallic molecules. (A) V^{IV}OFe^{II} → V^{V}OFe^{I} MMCT absorption of complex [(TMTAA)V^{IV}OFe^{II}Py$_5$Me$_2$]$^{2+}$ (TMTAA = 7,16-dihydro-6,8,15,17-tetramethyldibenzo[*b*,*i*][1,4,8,11]tetraazacyclo-tetradecine; Py$_5$Me$_2$ = 2,6-bis(1,1-bis(2-pyridyl)ethyl)pyridine). The red-circled section of the shaded area, with deconvolution shown in the inset, is assigned to the MMCT absorption. Reproduced from ref. 28 with permission from the American Chemical Society. (B) Co^{II}OW^{VI} → Co^{III}OW^{V} metal-to-polyoxometalate absorption of complex [CoW$_{12}$O$_{40}$]$^{6-}$. Reproduced from ref. 29 with permission from John Wiley and Sons.

possesses a large extinction coefficient while the transition is not observed for the other systems. A related charge transfer process in polyoxometalate $[Co^{II}W^{VI}_{12}O_{40}]^{6-}$, a molecularly defined all-inorganic structure, involves a Co^{II} to W^{VI} metal-to-polyoxometalate charge-transfer transition in the blue spectral region (Fig. 4B).[29]

2.2 Back electron transfer kinetics

For engaging heterobinuclear units as light absorbers to drive CO_2 reduction or H_2O oxidation, electron (or hole) transfer from the excited MMCT state to the catalyst, or directly to a reactant, needs to compete successfully with back electron transfer of the light absorber. Early photocatalytic observations such as CO_2 splitting to CO at $ZrOCu^{I}$ units,[3] H_2O oxidation at a polynuclear unit consisting of the $TiOCr^{III}$ light absorber coupled to the IrO_x nanocluster catalyst,[12] oxidation of 2-propanol at $TiOCe^{III}$ [14] or methanol at $TiOMn^{II}$ sites,[16] and very recently CO_2 reduction at $ZrOCo^{II}$ units[7] showed that lifetimes of the excited MMCT state are sufficiently long for electron transfer to the reactant or the multi-electron catalyst to proceed quite efficiently. Transient optical absorption studies of the TiOMn system allowed us to monitor back electron transfer directly and propose a detailed pathway.[9,18] For the spectroscopic study, the TiOMn unit was chosen because Mn^{II} possesses a spin and orbital forbidden ligand field absorption in the visible ($^6A_{1g} \rightarrow {}^4T_{2g}$) that is weak and unstructured thereby simplifying interpretation of transient optical spectra associated with MMCT excitation.

Excitation of the $Ti^{IV}OMn^{II} \rightarrow Ti^{III}OMn^{III}$ transition with 8 nanosecond (ns) laser pulses in the spectral region 425–535 nm spectral region revealed a bleach of the MMCT band that recovered with an average rate constant of 1.8 ± 0.3 μs (Albery model, $\gamma = 2 \pm 0.2$).[9] Hence, the room temperature back electron transfer is remarkably slow for such a small charge transfer chromophore. These first transient absorption experiments were conducted with TiMn–SBA-15 powders suspended in an index matching liquid in order to allow probing in transmission mode (powders or pressed wafers of mesoporous silica particles, which are typically approx. 1 micron sized, strongly scatter visible light). To understand the origin of the slow back electron transfer rate, the temperature-dependence of the rate needs to be determined. Reliable temperature dependent measurements are only feasible with samples held in a vacuum or a gas atmosphere, which requires optical transparency for spectroscopy in transmission mode. By anchoring TiOMn units on spherical silica nanoparticles (12 nm diameter, TiOMn loading approx. 0.5 mol% relative to Si) and pressing them into wafers, optically translucent samples were obtained. These preparations not only opened up transient absorption spectroscopic studies in vacuum, but also afforded a tenfold higher spectral sensitivity compared to experiments with index matching liquids. As a result, the weak Ti^{III} ($^2E \rightarrow {}^2T$) absorption with a maximum at 580 nm formed upon excitation of the MMCT transition could be detected, as shown in Fig. 5A.[18] The pump wavelength dependence of the Ti^{III} absorption (Fig. 5C) mirrored the MMCT absorption profile, which confirms that the observed Ti^{III} signal is formed by the excitation of the $Ti^{IV}OMn^{II} \rightarrow Ti^{III}OMn^{III}$ charge transfer transition.

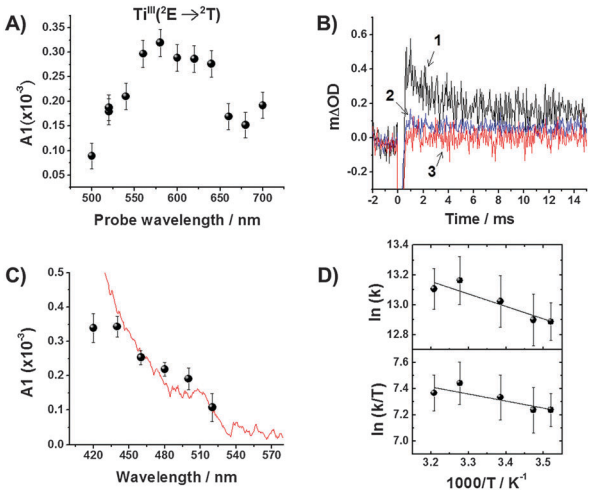

Fig. 5 Transient optical spectroscopy of the excited MMCT state of the TiOMn unit anchored on SiO_2 nanoparticles. (A) Transient absorption of the Ti^{III} center of the excited MMCT state. (B) Decay of Ti^{III} absorption at 580 nm upon excitation of MMCT with a 420 nm laser pulse of 8 ns duration (trace 1). The signal is not observed in the absence of MMCT as shown for SiO_2 particles with anchored Ti (trace 2) or Mn only (trace 3). (C) Laser pump wavelength dependence of the Ti^{III} absorption signal at 580 nm. (D) Temperature dependence of the decay kinetics of Ti^{III} transient absorption at 580 nm in the range of 10–40 °C. Plots of ln(k) (top) and ln(k/T) as a function of inverse temperature. Reproduced from ref. 18 with permission from the American Chemical Society.

The decay constant of the signal of 2.43 ± 0.20 μs at 295 K shown in Fig. 5B agreed with the long lifetime observed for the MMCT bleach.

The optical coupling constant of 4200 cm^{-1} derived from a Gaussian fit of the MMCT absorption profile based on Hush theory implies a strong coupling of the initially excited MMCT state with the ground state.[18] The large value agrees well with those observed for a wide range of mineral oxide based MMCT chromophores[19–26] as well as synthetic Prussian blue and related binuclear systems as discussed in more detail below, implying that there is an ultrafast back electron transfer pathway for the initially excited MMCT state. By contrast, a weak temperature dependence of the back electron transfer constant, shown in Fig. 5D, revealed a moderate activation energy of 1.67 ± 0.36 kcal mol^{-1} and a small pre-exponential factor of $(7.3 \pm 4.4) \times 10^{-6}$ s^{-1}, from which an activation enthalpy of 1.07 ± 0.36 kcal mol^{-1} and an activation entropy of -29.2 ± 1.2 cal K^{-1} mol^{-1} are derived. These values mean that the slow back electron transfer is not caused by a large activation barrier.

Determination of the electronic coupling constant from the temperature dependence of the back electron transfer rate by semi-classical Marcus theory gave a very small coupling constant $H = 0.64$ cal mol^{-1} (0.22 cm^{-1}).[18] The several orders of magnitude lower value of the coupling constant determined from the kinetic measurements compared with the coupling constant from the optical spectrum implies that back electron transfer occurs from a different electronic state than the initially prepared Frank–Condon state. This strongly indicates fast spin conversion following excitation of the initial MMCT

state prior to back electron transfer to the ground state and suggests the mechanism proposed in Fig. 6. Photon absorption by the $TiOMn^{II}$ ground state ($S = 5/2$ according to EPR measurements)[16] results in a high spin $S = 5/2$ excited MMCT state. Spin conserved back electron transfer from this initial excited state to the ground state (rate constant k_{BET1}) competes with intersystem crossing to a low spin $Ti^{III}OMn^{III}$ state (k_{ISC}). Spin flip could either take place on Ti or on Mn (d^4 $S = 2 \rightarrow d^4$ $S = 1$), or on both simultaneously. Our experimental finding that most of the dozen heterobinuclear MMCT units reported to date are photocatalytically active points to slow back electron transfer as a common property for these chromophores. Because spin flip on Ti or Zr is accessible to any unit featuring these acceptor centers, fast spin flip on the group 4 metal is the most probable intersystem crossing mechanism. The quantum efficiency of 20 percent or higher estimated for the fraction of excited TiOMn MMCT units with a lifetime of 2 μs means that the initially excited $S = 5/2$ high spin state branches on the ultrafast timescale between spin allowed back electron transfer to the ground state and intersystem crossing to a low spin $S = 3/2$ or 1/2 MMCT state. A unique property of all-inorganic binuclear units anchored on silica surfaces that may favor intersystem crossing over ultrafast spin conserved back electron transfer is the very strong polarization of the local silica environment induced by MMCT excitation (charge changes by a full unit on both metal centers, with no electron rich organic ligands available to partially compensate for the large electrostatic effect). Such polarization likely results in local restructuring of the silica ligand environment and therefore would slow down back electron transfer (k_{BET1}), thus enhancing the branching in favor of intersystem crossing. Once thermally relaxed in the low spin $Ti^{III}OMn^{III}$ state, the required spin flip for back electron transfer to the high spin $Ti^{IV}OMn^{II}$ ground state slows down the process (k_{BET2}) and explains the observed microsecond time constant. This renders charge transfer to a catalyst competitive with back electron transfer.

The slow back electron transfer of the excited TiOMn unit may seem unusual, yet there are precedents among molecular as well as solid state heterobinuclear MMCT systems, all traced back to ultrafast intersystem crossing following optical excitation of the initial charge transfer state. For molecular spin crossover complexes of first row transition metals like Fe^{II}, intersystem crossing rates of 10^{12}–10^{13} s^{-1} have been measured by transient optical absorption and femtosecond soft X-ray spectroscopy.[30–32] Ultrafast intersystem crossing of the Cr center of molecular RuCr MMCT complexes $[(NH_3)_5Ru(CN)Cr(CN)_5]$ and *trans*-$[(ms\text{-}Me_6[14]aneN_4)Cr((CN)Ru(NH_3)_5)_2]^{5+}$ to a different spin state for which transition to the ground state is spin forbidden was considered responsible for the slow, microsecond back electron transfer time constant.[33,34] For RuCo MMCT complexes $[(bpy)_2Ru(bb)Co(bpy)_2]^{5+}$ (bb is 1,2-bis(2,2′-bipyridyl-4-yl)ethane)[35] and CoFe or CoRu MMCT complexes $[LCo^{3+}(NC)M^{2+}(CN)_5]^-$ (M = Fe, Ru, L = pentadentate macrocyclic pentaamine ligand),[36] relatively slow nanosecond back electron transfer originates from ultrafast intersystem crossing at the Co center. The initially excited MMCT state produces a low spin Co^{II} that converts to the more stable high spin Co^{II} on the ultrafast timescale, resulting in slow spin forbidden back electron transfer to the MMCT ground state, which has low spin Co^{III}. For the latter process, a back electron transfer constant of 25 ns was observed and a small coupling constant of 8 cm^{-1} was calculated.[35] Likewise, the Prussian blue analogues exhibit metastable spin states upon excitation of the MMCT absorption band. At low temperatures the material $K_{0.2}Co_{1.4}[Fe(CN)_6]\cdot 6.9H_2O$ was found to exhibit a low spin state $Fe^{2+}(S = 0)$–CN–$Co^{3+}(S = 0)$ which converts to the high spin state $Fe^{3+}(S = 1/2)$–CN–$Co^{2+}(S = 3/2)$ upon excitation of the Fe^{2+}–Co^{3+} MMCT transition.[37,38] Activation parameters for these systems are $E_A \sim$ 2000–3000 cm^{-1} and pre-exponential factors of $\sim 8 \times 10^6 - 3 \times 10^9$ s^{-1},[39–42] similar to those observed for TiOMn.

The long lifetime of the excited TiOMn charge transfer state makes these heterobinuclear light absorbers suitable for driving multi-electron catalysts for CO_2 reduction and H_2O oxidation.

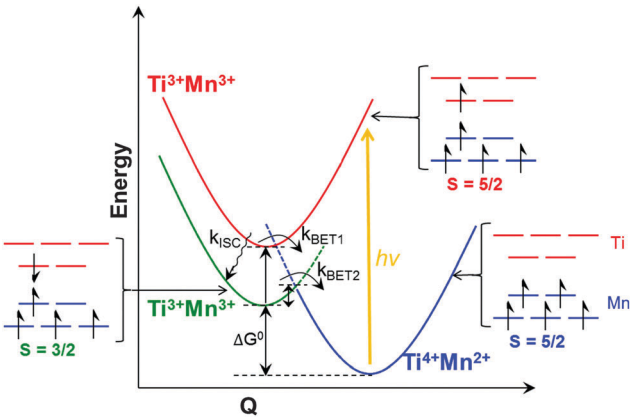

Fig. 6 Proposed mechanism of back electron transfer of the TiOMn metal-to-metal charge-transfer unit. Symbols are explained in the text. Adapted from ref. 18 with permission from the American Chemical Society.

2.3 Coupling of the binuclear light absorber to the nanocluster catalyst for CO_2 reduction

Two heterobinuclear units have thus far been found to reduce CO_2 to CO at the gas–solid interface upon photoexcitation of the MMCT state, namely $ZrOCu^{I}$ and $ZrOCo^{II}$.[3,7,17] For the $ZrOCu^{I}$ unit supported on mesoporous silica used in half reaction mode, the Cu center was stoichiometrically oxidized to Cu^{II} and no sacrificial donor was required. However, the CO product was trapped by strong binding to remaining Cu^{I} centers inside the silica pores, and no free CO was obtained. By contrast, MMCT driven reduction of CO_2 gas exposed to $ZrOCo^{II}$ units (Fig. 3) using 420 nm and shorter wavelength light produced gas phase CO, as expected based on the much weaker interaction of CO with Co^{II} centers. We have found by time-resolved FT-IR spectroscopic monitoring that CO escapes from the silica mesopores in 300 μs at room temperature.[43] However, unlike $ZrOCu^{I}$, the photo-reduction with $ZrOCo^{II}$ units required the presence of a sacrificial donor such as di- or triethylamine. Apparently, for this binuclear chromophore,

reduction of transient Co^{III} back to Co^{II} by a sacrificial donor upon Zr^{IV}–O–Co^{II} → Zr^{III}–O–Co^{III} excitation is necessary in order for transient Zr^{III} to be sufficiently long lived for activating adsorbed CO_2. A consequence of using the alkylamine donor is that formate is generated along with CO, which is due to the reactivity of the oxidized amine species that is formed upon electron donation.[7]

While photoexcited $ZrOCu^{I}$ and $ZrOCo^{II}$ units afford the direct splitting of CO_2 to CO, the chemistry is limited to 2-electron reduction products. However, an important goal of artificial photosynthesis is to accomplish the reduction of CO_2 by 4 or more electrons for the generation of energy dense products including liquid fuels like methanol. Because of their robustness, multi-electron catalysts in the form of inorganic particles are of particular interest. Metallic Cu has long been known from electrochemical studies to afford more highly reduced C_1 products like methanol or methane, and even species with 2 or more CC bonds.[44–46] Intense recent efforts in a growing number of labs to lower the overpotentials and improve product selectivity have revealed insights into how the nanostructure, morphology, or oxidation/reduction pretreatment of Cu catalysts can boost electrocatalytic efficiency.[47–54] Particularly promising for decreasing overpotentials and extending the degree of multi-electron reduction of CO_2 are Cu oxide nanoparticle catalysts, for which formaldehyde and methanol have been reported under photocatalytic conditions.[55,56]

We have developed a photodeposition method for the directed assembly of the $ZrOCo^{II}$ group and a cuprous oxide nanocluster that results in proper coupling of the catalyst to the Zr acceptor center of the light absorber. This single photon/single electron light absorber–multielectron catalyst assembly enables the exploration of higher reduction products of CO_2 by well defined all-inorganic units.

The synthetic step that enables the proper coupling of the cuprous oxide nanocluster to the acceptor metal of the light absorber is photo-driven deposition of Cu centers at the Zr terminus of the ZrOCo unit, as shown in Fig. 7. When loading the channels of mesoporous silica SBA-15 with the $Cu^{II}(NCCH_3)_4$ precursor with its weakly bound ligands and illuminating the $ZrOCo^{II}$ MMCT transition with visible light in the presence of triethylamine as a sacrificial electron donor, the photoexcitation introduces spatial directionality by exclusively reducing Cu^{II} centers in the electron transfer distance (in a vacuum) from transient Zr^{III}. Monitoring of the photoreduction by optical spectroscopy shows that Cu^{II} is converted to Cu^{I} (Fig. 7) while FT-IR spectroscopy indicates the concurrent loss of CH_3CN ligands.[57] Upon subsequent heating of the sample in the presence of oxygen gas, Cu oxide nanoclusters of 3 nm size are formed as can be seen by TEM imaging and energy dispersive X-ray (EDX) analysis (Fig. 7). While the spatial arrangement of the clusters with respect to the ZrOCo unit cannot be evaluated by spectroscopic measurements, photocatalytic results confirmed that ZrOCo chromophores are electronically coupled to Cu oxide clusters. The critical step that results in the assembly of the Cu oxide nanocluster adjacent to the acceptor center is most probably the detachment of CH_3CN ligands from the Cu center

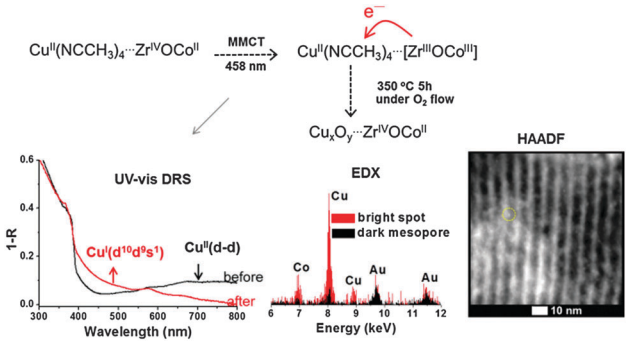

Fig. 7 Spatially directed assembly of the Cu oxide nanocluster catalyst coupled to the ZrOCo light absorber. UV-vis diffuse reflectance spectra show the reduction of the $[Cu^{II}(NCCH_3)_4]^{2+}$ precursor loaded in ZrOCo SBA-15 (black trace) upon photoexcitation of the ZrOCo charge transfer state to Cu^{I} (red trace). High angle annular dark field (HAADF) image of the sample after calcination reveals the formation of 3 nm sized Cu oxide clusters (bright spots). The white strips are the 2 nm thick walls of the 8 nm diameter channels of SBA-15. Energy dispersive X-ray spectra (EDX) of bright spots confirm the presence of Cu oxide clusters. Adapted from ref. 57 with permission from the American Chemical Society.

upon electron transfer from transient Zr^{III} observed by FT-IR spectroscopy. $Cu^{II}(NCCH_3)_4$ complexes in the vicinity interact preferentially with the ligand-deficient Cu^{I} so formed, which serves as a nucleus for cluster growth upon calcination to form a cupric oxide cluster adjacent to the Zr site of the ZrOCo chromophore.[57]

Proper electronic coupling of the light absorber and the catalyst was confirmed by the observed reduction of surface Cu centers upon photoexcitation of the ZrOCo unit. By exploiting the distinct infrared frequency dependence of adsorbed CO probe molecules on the Cu oxidation state to monitor the electronic state of surface Cu sites (^{13}CO mode at 2095 cm^{-1} for Cu^{II} and 2056 cm^{-1} for Cu^{0}), illumination of ZrOCo was found to efficiently convert Cu^{II}, the predominant oxidation state of surface centers upon calcination, to Cu^{0}.[57] Furthermore, CO_2 photoreduction rates upon loading of the Cu_xO_y–ZrOCo containing mesoporous silica with CO_2 gas were found to be controlled by the oxidation state of surface Cu centers. Catalyst clusters with Cu^{0} sites exhibit three times higher initial rates of CO evolution from CO_2 compared to clusters with predominantly Cu^{II} surface centers, as shown by the growth of gas phase CO infrared bands (Fig. 8A and B) along with the adsorbed CO product. The reactive CO_2 species was directly observed and identified as weakly adsorbed CO_2 on Cu^{0} in the form of a carboxylate, with a band at 1682 cm^{-1} ($^{13}CO_2$, 1656 cm^{-1}) as shown in Fig. 8C and D. The strong dependence of the CO_2 photoreduction yield on the oxidation state of the surface Cu centers constitutes direct proof that the ZrOCo group absorbs light under separation of charge, driving the catalysis on the Cu oxide multielectron catalyst by sequential transfer of electrons *via* transient Zr^{III} as illustrated in Fig. 9. The mechanism is further supported by the strong dependence of the CO_2 photoreduction efficiency on the redox potential of the acceptor (Zr *versus* Ti) and the photolysis wavelength used

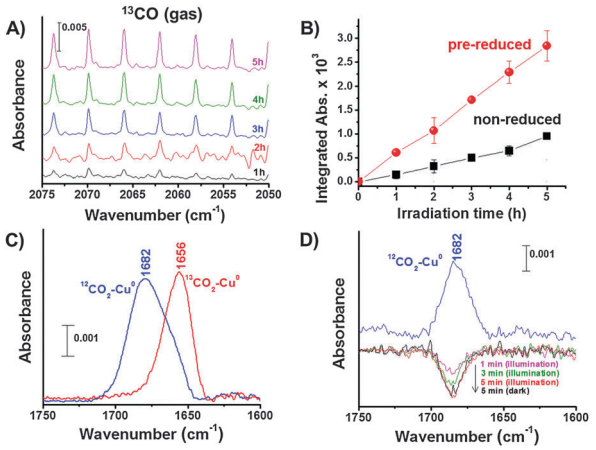

Fig. 8 Photoreduction of CO_2 gas by the Cu_xO_y–ZrOCo unit. (A) Difference FT-IR spectra of gas phase ^{13}CO growth upon 355 nm irradiation (100 mW cm^{-2}) in the presence of the 0.5 Torr diethylamine donor. (B) Growth kinetics of ^{13}CO (2065.9 cm^{-1} band) for Cu_xO_y–ZrOCo units with predominantly surface Cu^0 (red) and surface Cu^{II} (black). (C) Infrared mode of $^{12}CO_2$ and $^{13}CO_2$ adsorbed on the Cu^0 surface. (D) Consumption of surface $^{12}CO_2$ species upon photoreduction of CO_2 to CO. Blue, adsorbed $^{12}CO_2$ after loading of gas. Subsequent traces show reactant depletion during photocatalysis. Reproduced from ref. 57 with permission from the American Chemical Society.

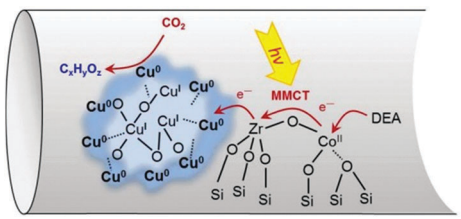

Fig. 9 Heterobinuclear ZrOCo^{II} light absorber coupled to the cuprous oxide nanocluster catalyst on the mesoporous silica surface. Separated charges generated by light absorbed by the MMCT unit result in the sequential transfer of electrons to the catalyst cluster where surface CO_2 is reduced. Reproduced from ref. 57 with permission from the American Chemical Society.

for MMCT excitation.[57] The search for more reduced products of CO_2 is in progress.

2.4 Coupling of the light absorber to the CO_2 reduction catalyst in other hetero-polynuclear assemblies

Coupling of molecular light absorbers with multi-electron catalysts for fuel generation under minimal loss of energy or charge while transferring electrons at rates that keep up with the solar flux is particularly challenging in the case of CO_2 reduction. The reason is the large discrepancy between the generally slow rate of CO_2 reduction catalysts and the much higher rate of photons at maximum solar intensity, with the catalytic turnover lagging behind the rate at which electrons are delivered. For the case of molecular light absorbers coupled to nanoparticle catalysts, the problem is mitigated by the very large number of available catalytic surface sites. While absorption of photons and flow of electrons to the catalyst particle far outpace the catalytic turnover at any given surface site, the large abundance of sites ready to start a new turnover compensates for the slow catalytic rate per site.

Reports in the literature on the coupling of molecular light absorber–CO_2 reduction catalysts focus primarily on covalent linkages between organometallic moieties for light absorption and catalysis. Ishitani has developed architectures for hetero-multinuclear assemblies consisting of Ru based bipyridyl complexes for visible light absorption linked to Re diamine catalysts for the selective photoreduction of CO_2 to CO, such as the complex shown in Fig. 10A.[58–65] A key finding regarding the design of the covalent linkage was that high efficiency requires non-π-conjugated bridges because π-conjugated linkage of the diimine ligands of the metal centers through the bridge results in too strong coupling with the catalyst, which diminishes its reducing power. The highest photocatalytic efficiencies for CO_2 reduction were observed for the $-CH_2-CH_2-$ bridge or the $-CH_2-O-CH_2-$ bridge, which provide weak yet adequate electronic coupling between light absorbing and catalytic moieties.[60,61]

Attachment of the molecular light absorber and the CO_2 reduction catalyst to a semiconductor particle surface offers both architecture for the half reaction unit and proper electronic coupling by through-particle electron transfer if the conduction band is situated energetically between the excited electron energy of the light absorber and the potential of the catalyst. The conduction band may offer an extended lifetime of injected electrons and accumulation of multiple charges as observed for the case of TiO_2, which could be essential for certain multi-electron catalysts to work efficiently.[66,67] In practice, a visible light sensitizer and a catalyst are randomly anchored on the semiconductor surface. Highly efficient and completely selective visible light driven reduction of CO_2 to CO was demonstrated using this approach for coupling the $Ru(bpy)_3$ light absorber *via* the TiO_2 particle to carbon monoxide dehydrogenase (Fig. 10B).[68–70] Similarly, an organic sensitizer-TiO_2–Re^I catalyst assembly proved as an efficient visible light photosystem for CO_2 splitting to CO.[71]

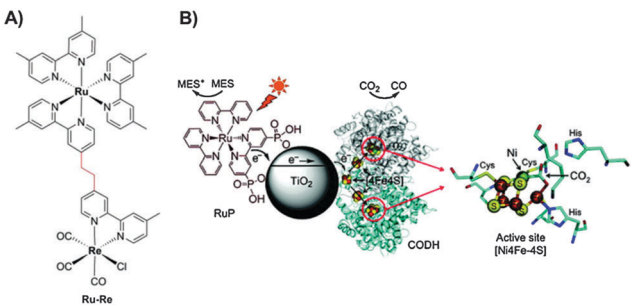

Fig. 10 Heteropolynuclear light absorber–CO_2 catalyst assemblies. (A) Heterobinuclear organometallic Ru^{II}–Re^I unit for visible light CO_2 reduction featuring an ethane bridge for optimal electronic coupling. Reproduced from ref. 63 with permission from the Royal Society of Chemistry. (B) Coupling of visible light sensitizer $Ru(bpy)_3$ phosphonate with two-electron CO_2 reduction catalyst Ch CODH I (enzyme) mediated by the TiO_2 particle that serves as an electron mediator and as an anchoring unit. Reproduced from ref. 68 with permission from the American Chemical Society.

3. Closing the photosynthetic cycle on the nanoscale

3.1 Photo-induced CO_2 reduction by H_2O at the ZrOCo chromophore coupled to the Ir oxide nanocluster catalyst

From an energetic standpoint, transient Co^{III} generated by $Zr^{IV}OCo^{II} \rightarrow Zr^{III}OCo^{III}$ excitation should have sufficient potential for driving a water oxidation catalyst, thus allowing for the desired replacement of the sacrificial donor by H_2O as an electron source. By using the photodeposition approach demonstrated for the directed assembly of the Cu_xO_y–ZrOCo unit discussed above, we explored the spatially controlled assembly of the Ir oxide nanocluster coupled to the Co donor site of the ZrOCo group. Ir oxide nanoclusters are known as very efficient O_2 evolving catalysts.[72–74] If proper coupling can be achieved, such a ZrOCo–IrO_x construct would allow closing of the photosynthetic cycle on the nanoscale by an all-inorganic, oxide-based assembly featuring a molecularly defined light absorber.

The approach for photodeposition of Ir oxide nanoclusters was inspired by our previous observation that an IrO_x cluster coupled to the Cr donor center of a TiOCr unit could be assembled by exposing the $Ir(acac)_3$ (acac = acetylacetonate) precursor in toluene solution in the dark to $TiOCr^{V}$ units in mesoporous silica. The $Ir^{III}(acac)_3$ underwent spontaneous electron transfer with the strongly oxidizing Cr^{V} center, forming $[Ir^{IV}(acac)_2]^{2+}$ under the loss of the acac ligand (the same process was also observed upon spontaneous reaction of $Ir^{III}(acac)_3$ with Cr^{VI} centers).[12,13] Subsequent mild calcination led to cluster formation around the ligand-deficient Ir^{IV} centers that served as the nucleus for growth, producing IrO_x nanoclusters of 2 nm diameter. The resulting $TiOCr^{III}$–IrO_x subsystems afforded visible light induced water oxidation to O_2 in neutral aqueous solution when run as half reaction with persulfate as a sacrificial acceptor.[12] While the Co^{II} center of $ZrOCo^{II}$ does not have sufficient positive potential to spontaneously oxidize $Ir^{III}(acac)_3$, transient Co^{III} generated by visible or UV light excitation of the $Zr^{IV}OCo^{II} \rightarrow Zr^{III}OCo^{III}$ transition (Fig. 3) might undergo electron transfer with the Ir precursor. As shown in Fig. 11A and B, optical and FT-IR spectroscopy revealed photo-induced oxidation of the Ir^{III} to Ir^{IV} under elimination of the acac ligand at room temperature. Heating in an oxygen atmosphere led to the formation of 2 nm sized Ir oxide nanoclusters as observed by HAADF (high angle annular dark field) imaging, while the structural integrity of the ZrOCo chromophore was preserved.[75]

Photo-excitation of ZrOCo–IrO_x units (Fig. 12A) upon loading of a gas mixture of 760 Torr $^{13}CO_2$ and 100 mTorr H_2O into the SBA-15 sample (pressed wafer) at 355 nm resulted in the formation of ^{13}CO and O_2. Carbon monoxide was detected in the gas phase, as shown by the ro-vibrational spectrum of Fig. 12B. Mass spectrometric measurements confirmed the formation of oxygen gas, including isotopically labeled $^{18}O_2$ when using pure $H_2{}^{18}O$. Concurrent production of $^{16}O_2$ is due to the split-off O of $^{13}C^{16}O_2$ (Fig. 12C and D). No CO or O_2 was produced in the absence of water, further confirming that it is the electron source. Moreover, synthesis of IrO_x nanoclusters in ZrOCo functionalized SBA-15 without the photodeposition step

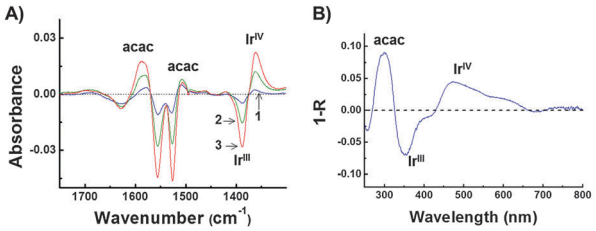

Fig. 11 FT-infrared and UV-vis spectra show the oxidation of the $Ir^{III}(acac)_3$ complex under the loss of the acac ligand upon photodeposition in ZrOCo–SBA-15 loaded with $Ir^{III}(acac)_3$. (A) Difference FT-IR spectra recorded before and after photodeposition (355 nm) for 10 min (trace 1), 30 min (trace 2), and 60 min (trace 3). (B) Difference UV-vis spectrum before and after photodeposition (355 nm) for 60 min. Growth of $[Ir^{IV}(acac)_2]^{2+}$ is denoted by Ir^{IV}, while acac denotes the formation of a detached free acetyl acetone ligand. Reproduced from ref. 75 with permission from the American Chemical Society.

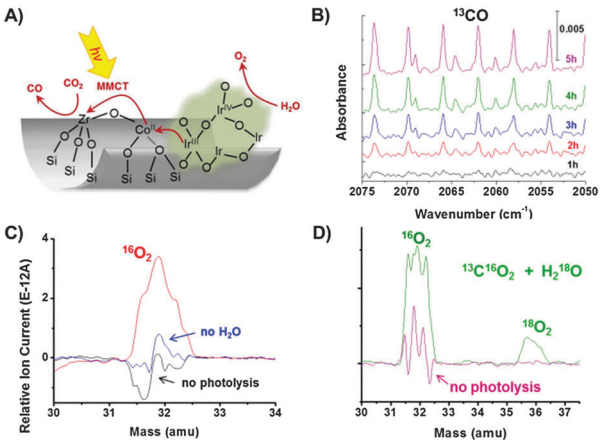

Fig. 12 Photoreduction of $^{13}CO_2$ by H_2O at ZrOCo–IrO_x units in SBA-15. (A) Light absorber–catalyst assembly. (B) Ro-vibrational FT-IR spectra of the growing gas phase ^{13}CO product upon irradiation at 355 nm in the presence of the $^{13}CO_2$ and H_2O gas mixture. (C) Mass spectroscopic monitoring of the O_2 product after irradiation of ZrOCo–IrO_x SBA-15 loaded with $^{13}CO_2$ and H_2O. (D) Oxygen monitoring of ZrOCo–IrO_x SBA-15 loaded with $^{13}C^{16}O_2$ and $H_2{}^{18}O$. Control spectra (sample without illumination and sample illuminated in the absence of H_2O) are also shown. Reproduced from ref. 75 with permission from the American Chemical Society.

did not result in CO_2 reduction by H_2O, demonstrating that the random formation of oxide clusters in the mesoporous silica does not lead to proper coupling of Co donor centers with the catalyst clusters. The result constitutes the first system for closing the photosynthetic cycle of CO_2 reduction by H_2O with an all-inorganic polynuclear cluster featuring a molecularly defined light absorber.

The quantum efficiency at 355 nm was estimated to be 17 percent, which indicates that hole transfer from the transient Co^{III} donor to the IrO_x cluster competes remarkably well with $Zr^{III}OCo^{III} \rightarrow Zr^{IV}OCo^{II}$ back electron transfer of the light absorber (Fig. 12A). In the case of the $TiOMn^{II}$ unit discussed in Section 2.2, the observed long lifetime of the excited $Ti^{III}OMn^{III}$ state of 2.4 μs at room temperature was explained by ultrafast intersystem crossing upon photo-excitation, resulting in slow back electron transfer due to the required spin-flip to regenerate the light absorber

ground state.[9,18] For the $ZrOCo^{II}$ unit, intersystem crossing from the initial high spin $Zr^{III}OCo^{III}$ $S = 3/2$ state to the low spin $S = 1/2$ excited MMCT surface would result in slow back electron transfer to ground state $Zr^{IV}OCo^{II}$ rendering hole transfer from Co^{III} to IrO_x competitive. With the electron of Zr^{III} blocked from transfer back to Co, the reduced Zr is rendered sufficiently long lived for electron transfer to adsorbed CO_2 to occur.

Available experimental data on the mechanism of water oxidation at the Ir oxide nanocluster surface are the observation of the O–O stretch mode of the IrOOH intermediate by rapid-scan FT-IR spectroscopy upon visible light sensitized water oxidation catalysis in aqueous solution (band at 830 cm^{-1} with appropriate ^{18}O and D isotopic shifts of a hydroperoxy group),[76] and the detection of Ir^V upon steady state electrocatalytic water oxidation at IrO_2 by ambient pressure XPS.[77] Taken together, the results suggest that the mechanism for O–O bond formation involves Ir^{IV} centers on the IrO_x nanocluster surface being oxidized by the first arriving hole to oxo Ir^V ($Ir^V{=}O$) followed by nucleophilic attack of H_2O on the oxo site to yield the $Ir^{III}OOH$ hydroperoxide intermediate. A surface IrOOH intermediate on $IrO_2(110)$ has been predicted by quantum chemical calculations.[78] A similar mechanism was proposed for mononuclear organo Ir catalysts for water oxidation.[79,80]

While no single electron catalytic intermediate has yet been observed for CO_2 reduction at transient Zr^{III}, the energetically most accessible species is the HOCO radical (hydroxycarbonyl, sometimes also termed hydrocarboxyl).[81] We propose the formation of HOCO followed by spontaneous dissociation into CO (which escapes rapidly from the silica mesopores into the gas phase) and OH radicals. The fate of OH depends on the specific reaction conditions.[3,7,82] For the ZrOCo–IrO_x system, mass spectroscopic monitoring of photocatalytic conversion of $^{13}C^{16}O_2$ and $H_2{}^{18}O$ shows that the departing ^{16}O upon reduction of carbon dioxide forms $^{16}O_2$ (Fig. 12D).

To absorb a sufficient fraction of the solar spectrum, use of 2-photon absorber systems is required. Hence, the $ZrOCo^{II}$ single light absorber needs to be replaced by two heterobinuclear units operating in tandem, *e.g.* $ZrOFe^{II}$–$TiOCo^{II}$. With the synthesis of the individual units already established,[11,15] our approach for the spatially directed assembly of the $ZrOFe^{II}$ unit with the Fe donor coupled to the Ti acceptor of the $TiOCo^{II}$ group will employ the photodeposition method introduced in Section 2.3.

3.2 Complete photosynthetic cycles with other systems

Development of complete, bias-free integrated systems for visible light driven photoreduction by water has gained increasing emphasis in the past several years, with most systems reducing protons to hydrogen (overall water splitting) using semiconductor components as light absorbers. Monolithic systems include visible light water splitting at triple junction amorphous silicon,[83,84] tandem cells made of III–V semiconducting materials,[85,86] WO_3 or Fe_2O_3 photoanode/dye sensitized[87] or $BiVO_4$/a-Si tandem cells,[88] and 2-photon TiO_2/Si nanowire or n-WO_3/np$^+$Si microwire arrays.[89–91] Recent solar water splitters include a Fe_2O_3/a-Si photoelectrochemical cell[92] and a perovskite photovoltaic-biased electrosynthetic system that operates at 12 percent power efficiency[93] (power efficiency is defined as the power stored in the photosynthetic products divided by the power of the incident solar light. For water splitting, this can be expressed as (1.23 V)(J)/P, where J is the operational photocurrent density in Å cm^{-2} and P is the incident irradiance in W cm^{-2}).[84] These visible light water splitting systems close the photosynthetic cycle on the macroscale. Among them, only one features a membrane for separating the evolving hydrogen from oxygen.[86] Colloidal semiconductor nanoparticles in aqueous solution functionalized by cocatalysts, either single or dual bandgap, complete the photocatalytic cycle on the nanoscale.[94–98] These systems are promising although they currently lack the hierarchical arrangement of components needed for product separation, which also holds for biomolecular–semiconductor hybrid assemblies operating in 2-photon mode.[99]

For CO_2 photoreduction by H_2O, early single integrated systems were large bandgap metal oxide particles absorbing UV light,[100–103] which was followed by considerable effort to functionalize these materials with metal or metal oxide cocatalysts and explore various particle morphologies.[103–107] Coupling of two semiconductor materials in tandem (Z-scheme) mode extends the light response into the visible region, and a $SrTiO_3$/InP monolith functionalized with a molecular CO_2 reduction catalyst was recently reported to generate formate at 0.1 percent efficiency.[108] Using a triple junction semiconductor as a visible light absorber similar to the case of water splitting discussed above coupled to noble metal co-catalysts for CO_2 reduction and H_2O oxidation, 4.6 percent power efficiency for CO_2 to formate conversion was achieved[109] (in photovoltaic-electrochemical cell configuration using triple junction perovskite PV elements and noble metal electrodes for CO_2 reduction and H_2O oxidation, a power efficiency of 6.5 percent for the reduction of CO_2 to CO was achieved).[110] Demonstration of UV light driven CO_2 reduction by H_2O at isolated tetrahedral Ti centers in mesoporous silica[82,111] gave us the inspiration to replace the Ti–O ligand to metal charge transfer (LMCT) chromophore with visible light absorbing MMCT chromophores in which an electron is donated by a second metal rather than an O ligand, which was the starting point of the development of heterobinuclear units as all-inorganic molecularly defined light absorbers.[3,4]

Integrated photo-driven systems of entirely molecular nature for the direct reduction of CO_2 by H_2O have not yet been demonstrated, but exciting new developments on molecular subsystems for the H_2O oxidation or CO_2 reduction half reactions have been reported. These molecular subsystems are integrated with semiconductor components in visible light driven photoelectrochemical cells.[80,112–115] On the water oxidation side, recent approaches by several groups for addressing the challenge of efficiently coupling a molecular light absorber with a multielectron water oxidation catalyst are guided by the tyrosine mediator design of Nature's Photosystem II.[116] In a series of studies by the Mallouk group in collaboration with the groups of Moore, Moore and Gust, an Ir oxide nanocluster was coupled to a $[Ru(bpy)_3]^{2+}$ or a porphyrin visible light absorber through a benzimidazole-phenol redox relay with both components

covalently anchored on a TiO_2 surface, as shown in Fig. 13A. The assembly mimics the tyrosine–histidine bridge between the Mn_4O_4 catalyst and the P_{680} chromophore of Photosystem II. Detailed insights into the competing charge transfer processes were obtained by transient optical spectroscopy.[117–120] Upon absorption of a visible photon by the Ru chromophore and ultrafast injection of an electron into TiO_2, transfer of an electron from the benzimidazole-phenol mediator to the oxidized Ru complex reduces the oxidized chromophore on a short timescale compared to the catalytic turnover of O_2 at the IrO_x particle. As a result, the competition between undesired transfer of electrons injected into TiO_2 back to the oxidized light absorber and hole injection into the IrO_x catalyst is shifted in favor of catalysis, thus improving the quantum efficiency of water oxidation by a factor of three. The approach offers substantial room for further efficiency improvement because the relative position of the light absorber and the catalyst with the attached mediator is not yet molecularly defined in the present system.[117] A first example of a covalent linkage of the benzimidazole-phenol relay to a porphyrin light absorber shown in Fig. 13B has been demonstrated, although not yet coupled to a water oxidation catalyst.[120] Transient optical and pulsed EPR spectroscopy confirmed proton-coupled electron transfer of the link upon hole injection from the sensitizer yielding a benzimidazolium-phenoxyl radical species. Concerted proton transfer accompanying the arrival of the hole from the light absorber situates the redox potential of the relay between the potential of the catalyst and the chromophore, an essential requirement for efficient photocatalysis.[120]

The important role of redox mediators in molecular light absorber–oxygen evolving molecular catalyst assemblies was investigated for tyrosine-type constructs by the groups of Hammarstroem and Styring.[121] The detailed dynamics of proton-coupled electron transfer and hydrogen bond adjustment within the relay unit uncovered by this study led to an understanding of how the processes assist in accomplishing a minimum energy pathway for charge transport between the light absorber and the catalyst. For an assembly consisting of a $[Ru(bpy)_3]^{2+}$ light absorber covalently linked to a tyrosine–histidine mediator/organo di-manganese unit shown in Fig. 14, up to three sequential photon absorption-charge separation steps allowed the model catalyst to advance from the Mn^{II},Mn^{II} state to the Mn^{III},Mn^{IV} state although no water oxidation activity has been reported so far.[122]

The rapidly expanding variety of molecular light absorber–catalyst assemblies for water oxidation with visible light is reflected in systems like $[Ru(bpy)_3]^{2+}$ coupled to a mononuclear Ru catalyst embedded in a layer of Nafion[123] or a porphyrin chromophore driving a molecular Ir^{III} catalyst co-anchored on a TiO_2 surface (Fig. 15A).[124] The $[Ru(bpy)_3]^{2+}$ light absorber was used for driving a Ru polyoxotungstate catalyst with the components coupled through strong electrostatic interactions, which gave very fast hole transfer times of 1 ns.[125,126] The advantage of a saturated alkane spacer for optimal electronic coupling between the molecular chromophore and the catalyst, already noted for the coupling of a CO_2 reduction catalyst (Section 2.4), was realized in the water oxidation subsystem shown in Fig. 15B

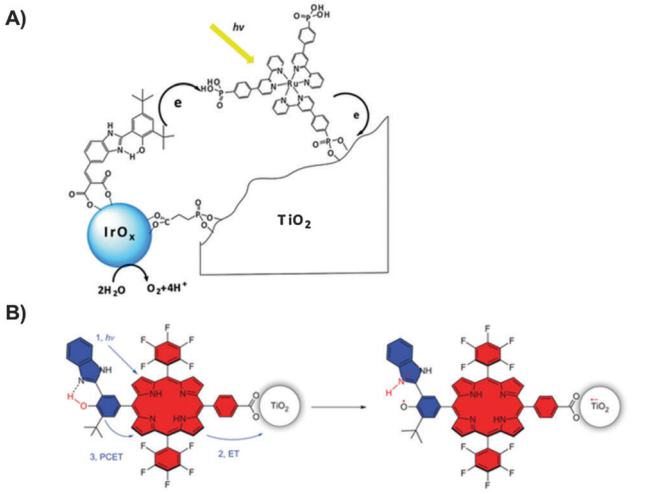

Fig. 13 Efficiency of molecular light absorber–catalyst assemblies for water oxidation boosted by the redox mediator. (A) Benzimidazole-phenol redox relay for increasing the quenching rate of the oxidized Ru light absorber. Reproduced from ref. 117 with permission from the National Academy of Sciences of the United States of America. (B) The same type of mediator linked to a porphyrin light absorber. Benzimidazolium-phenoxy radical species formed upon proton-coupled electron transfer temporarily stores positive charge generated on the porphyrin light absorber that otherwise would back react with electron injected into TiO_2. Reproduced from ref. 120 with permission from the Nature Publishing Group.

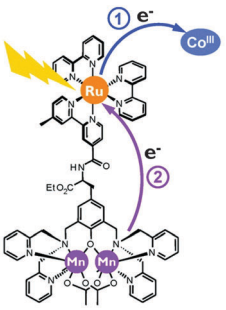

Fig. 14 Biomimetic tyrosine–histidene mediator enabling three sequential photo-induced electron transfer steps for oxidizing the organo-dimanganese catalyst from Mn^{II},Mn^{II} to Mn^{III},Mn^{IV} states. Reproduced from ref. 122 with permission from the American Chemical Society.

(methylene bridge in this case).[113,127] A different type of molecular assembly for water oxidation reported recently features a perylene dicarboximide chromophore linked to an organometallic Ir catalyst (Fig. 15C).[128] Recent progress in the efficient coupling of a molecular light absorber with a multi-electron catalyst on the CO_2 reduction side is discussed in Section 2.4.

4. Earth abundant inorganic oxide catalysts for water oxidation

4.1 Enhancing activity by nanostructuring of transition metal oxides

Ir oxide nanoclusters as efficient catalysts for water oxidation allowed us to assemble in a spatially directed fashion the

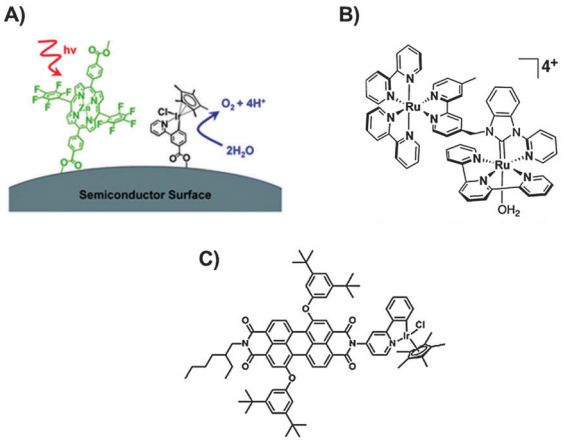

Fig. 15 Heteropolynuclear light absorber–H_2O oxidation catalyst assemblies: strategies for optimizing the coupling of molecular light absorbers to the water oxidation catalyst. (A) Co-anchoring of the Zn porphyrin chromophore and the Ir catalyst on the solid oxide surface. Reproduced from ref. 124 with permission from the Royal Society of Chemistry. (B) Methylene bridge for optimal electronic coupling of the Ru based light absorber–catalyst unit. Reproduced from ref. 127 with permission from the American Chemical Society. (C) System featuring the direct attachment of the organic light absorber to the catalyst without saturated linkage: perylene dicarboximide directly coupled to the Ir catalyst. Reproduced from ref. 128 with permission from the National Academy of Sciences of the United States of America.

ZrOCo–IrO_x unit for closing the photosynthetic cycle on the nanoscale,[75] yet Ir oxide is not a viable component for a scalable artificial photosystem because of the scarcity of this element.[129] Earth abundant metal oxides, in particular those of first row transition metals, offer robust alternatives. Estimates based on early reports of electro- or light-driven Co and Mn oxide catalysts[130–145] showed turnover frequencies (TOFs) per metal center in the range 10^{-4} to 10^{-2} O_2 s^{-1} at overpotentials in the 300–400 mV range depending on the structure, pH and temperature conditions,[146–149] which are at least two orders of magnitude lower than TOF of IrO_2 clusters at similar overpotential.[73,74,150] Intense efforts in the past several years to enhance the TOF per projected area of the catalyst (footprint) by nanostructuring of the metal oxide, particularly those of Co, Mn and Ni, have led to a dramatic increase of the TOF per projected catalyst area due to very large enhancements of the surface area and, in some cases, the increase of the intrinsic rate per surface metal center. Examples for crystalline Co and Mn oxides include nanostructuring by using mesoporous silica as a scaffold.[146–149] TOF enhancements for oxygen evolution per projected area of over 1000 at comparable overpotentials were achieved under close to neutral pH conditions. This large factor includes a 16 fold increase of the TOF per surface Co site in the case of crystalline Co_3O_4 nanorod bundles over micrometer sized Co_3O_4.[146] Expansion of the mesoporous silica scaffold approach using materials such as SBA-15 and KIT-6 structures led to further improvements of the activity of Co_3O_4 or Mn oxide nanocatalysts when left incorporated in the scaffold[151,152] or in the form of free nanoparticles.[153] Cubic or spherical Co_3O_4 nanocrystals supported on Ni foam,[154] in the form of colloids synthesized by novel methods such as pulsed laser ablation in liquids,[155] *in situ* phase transformation of layered Co alkoxy precursors,[156] or with nanochain morphology showed record activities especially in alkaline solution.[157] High surface area mesoporous Co_3O_4 electrocatalysts with high catalytic activity were obtained by hard templating with mesoporous silica followed by the removal of the template.[158,159]

Introduction of novel methods for the preparation of high surface area amorphous electrodeposits, in particular of Co oxide of type CoPi, on various electrodes has dramatically expanded the availability of this abundant metal oxide as a co-catalyst for a variety of different photosystems.[160,161] Nanostructured Mn oxide electrodeposits led to similar advancement of the use of this Earth abundant catalyst as both water oxidation and oxygen reduction catalysts.[162] Clearly, nanostructured first row transition metal oxides in a variety of morphologies have emerged as very promising water oxidation catalysts for incorporation into hierarchical structures for developing integrated artificial photosystems.

As will be discussed below (Section 5), we are developing a hierarchical nanostructured assembly for closing the photosynthetic cycle of CO_2 reduction by H_2O under membrane separation that utilizes high surface area Co_3O_4 in the form of nanotubes as water oxidation catalysts. The assembly consists of a macroscale array of separated, functionalized Co oxide–silica core–shell nanotubes, with each tube operating as an independent photosynthetic unit. For quantifying the catalytic activity of crystalline Co_3O_4 nanotubes, we initially prepared surfactant-free CoO nanotubes utilizing a modified solvothermal synthesis method.[163,164] Fig. 16A shows an Angstrom resolution TEAM (transmission electron aberration-corrected microscopy) image of a 12 nm diameter CoO nanotube. Calcination under low O_2 pressure resulted in the conversion to crystalline Co_3O_4 nanotubes as evidenced by the XRD data shown in Fig. 16B. Visible light induced water oxidation catalysis was evaluated using $[Ru(bpy)_3]^{2+}$ in combination with the $S_2O_8^{2-}$ sacrificial acceptor, a widely used aqueous photosensitization system.[165] Upon collision of the photo-generated mild oxidant $[Ru(bpy)_3]^{3+}$ of well-defined potential (+1.26 V) with a Co_3O_4 nanotube in close to neutral aqueous solution, a hole is transferred to the catalyst. Sequential transfer of four holes from $[Ru(bpy)_3]^{3+}$ to a particle

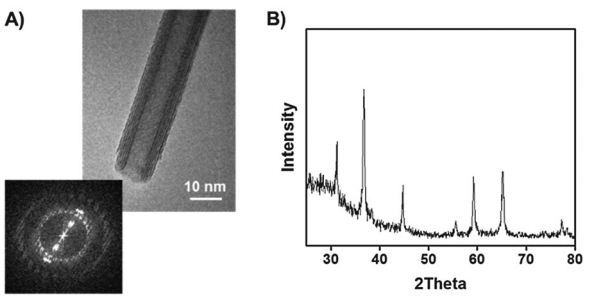

Fig. 16 Crystalline Co_3O_4 nanotube as a water oxidation catalyst. (A) TEAM image of the CoO nanotube with Fourier Transform showing a single crystal structure. (B) X-ray diffraction pattern of the Co_3O_4 nanotube after calcination. Reproduced from ref. 164 with permission from the Royal Society of Chemistry.

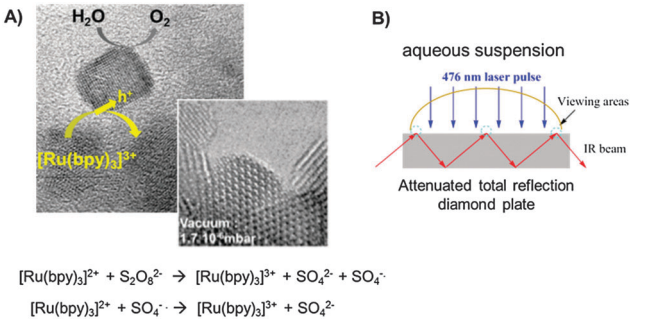

Fig. 17 Time-resolved ATR FT-IR spectroscopy of visible light driven water oxidation at Co_3O_4 nanoparticles. (A) Visible light sensitized charge injection method for driving the catalysis. TEAM images of single crystal Co_3O_4 particles (4 nm) are shown. (B) Measurement set-up. A suspension of Co_3O_4 particles containing a sensitizer is placed on a diamond ATR plate. Geometry of the visible light photolysis beam and the infrared probe beam is shown. Adapted from ref. 167 with permission from Elsevier Science Ltd.

converts two H_2O molecules to O_2 and $4H^+$ (Fig. 17A). Mass spectrometric analysis of O_2 evolving in the head space and electrochemical probing of dissolved O_2 (Clark electrode) gave a TOF of 0.018 O_2 s^{-1} per surface Co center, which was found within uncertainty to be the same as for 4 nm sized spherical Co_3O_4 nanocrystals shown in Fig. 17A.[164,166,167] Given a footprint of 1.13 nm^2 for a 12 nm diameter vertical nanotube, a tube of 700 nm length will be able to keep up with O_2 production even at maximum solar intensity.[147] Hence, the catalytic efficiency of the Co_3O_4 nanotube is of appropriate magnitude for use in an artificial photosynthetic assembly.

4.2 Mechanism of water oxidation at the Co_3O_4 catalyst surface

For guiding further improvement of the efficiency of the Co oxide catalyst and expanding the design space for catalyst structures and morphologies, we need to find out whether the TOF of 0.02 s^{-1} per surface Co center implies that all surface centers operate at a similar rate, or whether the value merely represents an average of widely different rates. Are there sites operating at much higher rates while others are slower or even inactive, and if so, what is the structure of the fastest sites? We seek to gain knowledge of the structure and kinetics of surface intermediates to learn about the nature of the rate limiting step, which may provide guidance for improving the catalytic efficiency through synthetic modification or catalyst pretreatment. To address these questions, we have utilized time-resolved FT-IR spectroscopy of aqueous suspensions of Co_3O_4 crystalline nanoparticles in the attenuated total reflection configuration (ATR), starting with the rapid-scan method. Time-resolved spectroscopic monitoring of catalysis requires pulsed initiation of the reaction. The $[Ru(bpy)_3]^{2+}$–$S_2O_8^{2-}$ visible light sensitization system in pulsed version offers a wide temporal window from steady state to ultrafast.

4.2.1 Spectroscopic observations. When illuminating an aqueous suspension (pH 7.5) of surfactant-free Co_3O_4 nanocrystals (4 nm) containing $[Ru(bpy)_3]^{2+}$ and the persulfate electron acceptor with a 476 nm laser pulse of 300 ms duration, two surface intermediates with distinct kinetic behavior were detected.[168] A superoxide species absorbing at 1013 cm^{-1} exhibits an O–O stretch mode that is characteristic for interaction with two surface metal centers.[169] Isotopically shifted bands at 995 and 966 cm^{-1} observed when conducting the experiment with unlabeled $Co_3{}^{16}O_4$ nanoparticles suspended in pure $H_2{}^{18}O$ (Fig. 18A, trace b) show a 1 : 1 ratio of superoxide $^{18}O^{16}O$ (995 cm^{-1}) and fully labeled $^{18}O^{18}O$ (966 cm^{-1}) after a single 300 ms light pulse. The superoxide $^{18}O^{16}O/^{18}O^{18}O$ ratio changes monotonously, from 1 : 1 to 1 : 8, for the subsequent four light pulses (total of 1500 ms visible light sensitization, inset of Fig. 18Ab). This directly reveals the stepwise exchange of surface hydroxyl groups by the coordination of $H_2{}^{18}O$ molecules upon photocatalytic cycling (there is no competing spontaneous (dark) exchange of surface OH groups of Co_3O_4 with bulk water, which is confirmed by the high (50 percent) yield of partially labeled $^{18}O^{16}O$ superoxide during the initial 300 ms photolysis period).[168] No unlabeled $^{16}O^{16}O$ superoxide is observed. A modest D isotope shift of the superoxide stretch when conducting the experiment in pure D_2O signals hydrogen bonding interaction with a neighboring hydroxyl group (Fig. 18A, trace c). Most of the rise of the superoxide intermediate occurs during the 300 ms illumination pulse, with continued growth after termination of the pulse until all hole-injecting $[Ru(bpy)_3]^{3+}$ species are consumed, as shown in Fig. 18B. The concentration of the superoxide so produced does not change appreciably in the subsequent dark period even on the several second timescale, which is to be expected given the known stability of superoxide species on metal surfaces. This 3-electron oxidation intermediate requires the delivery of one additional hole by continued illumination for liberating O_2 and restarting the catalytic cycle.

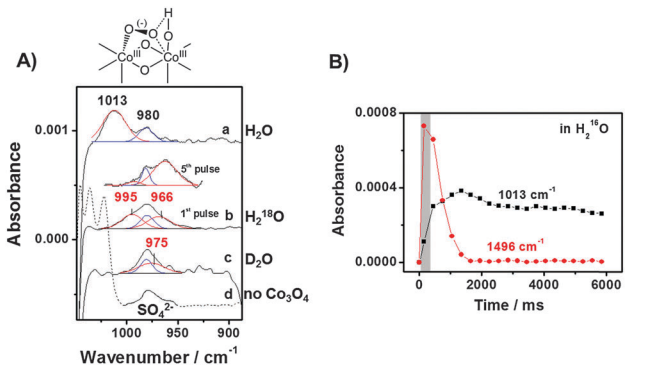

Fig. 18 Superoxide surface intermediate of water oxidation on the Co_3O_4 catalyst in aqueous solution observed by rapid-scan FT-IR spectroscopy. (A) Infrared absorption of O–O mode in (a) $H_2{}^{16}O$, (b) $H_2{}^{18}O$, (c) D_2O, and (d) control run without the catalyst at 5850 ms after the onset of 300 ms duration laser photolysis pulse. The inset of (b) shows the change of the superoxide $^{16}O^{18}O$–$^{18}O_2$ ratio after 1500 ms of illumination. (B) Kinetics of the superoxide surface intermediate (1013 cm^{-1}, black trace). The concurrent consumption of $[Ru(bpy)_3]^{3+}$ (1496 cm^{-1}, red trace) by hole injection into Co_3O_4 particles is also shown. The grey area corresponds to the illumination period. Reproduced from ref. 168 with permission from the Nature Publishing Group.

A substantial fraction of the catalytic sites completes the cycle after a 300 ms pulse as indicated by O_2 detected electrochemically using a Clark electrode, shown in Fig. 19A. Mass spectrometric analysis of the isotopic composition of the oxygen gas accumulating in the head space in experiments with pure $H_2{}^{18}O$ on the several minute timescale gave a ratio of 8 : 1 of fully labeled $^{18}O_2$ *versus* partially labeled $^{18}O^{16}O$ (and no unlabeled $^{16}O_2$, Fig. 19B). The agreement between the isotopic composition of the O_2 product and the superoxide intermediate after 5 light pulses (inset of Fig. 18Ab) constitutes compelling evidence that the surface superoxide is a kinetically relevant intermediate of the catalytic cycle for water oxidation by Co_3O_4.

The second transient infrared band observed at 840 cm^{-1} does not exhibit any isotopic shift when conducting the photocatalysis in $H_2{}^{18}O$ or D_2O (Fig. 20A), which points strongly to a Co^{IV}═O oxo intermediate[168] (resonant with oxyl Co^{III}–$O^{\bullet}$, which may more accurately reflect the electronic structure of the group).[170,171] In contrast to superoxide, the oxo species decreases spontaneously in the dark with a rate constant of 1 s^{-1} (Fig. 20B). Because the decay kinetics are slow compared to the rise of the superoxide species, the 840 cm^{-1} Co^{IV}═O intermediate cannot be the precursor of the observed superoxide at 1013 cm^{-1}. The 840 cm^{-1} oxo group therefore belongs to a much less active site that closes the O_2-producing catalytic cycle on at least a 150 times slower timescale.[168]

4.2.2 Proposed mechanism. Cyclic voltammetry analyses of various Co oxide films including electrocatalytic deposits on a range of anodes agree well with Pourbaix analyses of layered Co double hydroxides whose key structural motif is adjacent to oxo-bridged Co–OH groups, *i.e.* Co(OH)–O–CoOH. This catalytically most active structural phase is formed under electrocatalytic conditions at applied potentials required for O_2 evolution.[172] Oxo-linked octahedral Co^{III}–OH centers are prevalent on any crystallographic surface of Co_3O_4 terminated by hydroxyl groups.[172–174] Therefore, this is the most likely structural motif of the fast catalytic sites (it should be noted that water oxidation driven by a short 300 ms light pulse delivers a far too small number of charges for any restructuring

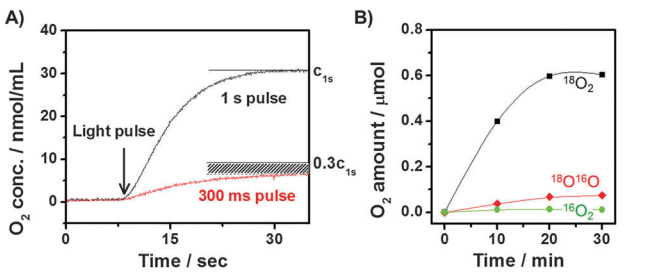

Fig. 19 Measurement of O_2 evolution. (A) Electrochemical monitoring of O_2 in solution in response to a single 476 nm light pulse. 300 ms duration pulse: red trace. 1 s duration pulse: black trace. The shaded section indicates the missing O_2 in the 300 ms experiment due to incomplete catalytic cycles arrested at an intermediate stage. (B) Isotopic composition of O_2 gas accumulated in the headspace of $H_2{}^{18}O$ solution measured by mass spectroscopy. Reproduced from ref. 168 with permission from the Nature Publishing Group.

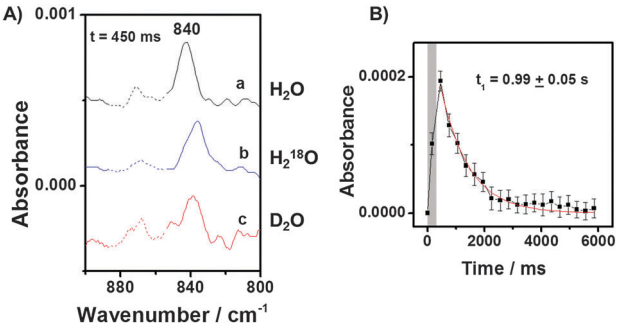

Fig. 20 Transient intermediate at 840 cm^{-1} attributed to the surface Co^{IV}═O site. (A) Infrared band at 450 ms after the onset of 300 ms laser photolysis pulse in (a) $H_2{}^{16}O$, (b) $H_2{}^{18}O$, and (c) D_2O. (B) Decay kinetics of the intermediate assigned to the nucleophilic attack of H_2O. The grey area corresponds to the illumination period. Reproduced from ref. 168 with permission from the Nature Publishing Group.

of the crystalline Co_3O_4 surface to occur. Restructuring near the surface is a phenomenon associated with an applied potential sufficient for driving water oxidation catalysis electrochemically,[175] as will be discussed further in Section 4.3). Tafel plot analysis of cobalt oxide films has been interpreted in terms of a fast pre-equilibrium preceding the OO bond-forming reaction in which a Co^{IV}(═O)–O–Co^{III}–OH resting state converts to Co^{IV}(═O)-O-Co^{IV}═O.[176] This step is supported by a computational study on the Co_4O_4 cubane model cluster.[177] Hence, the most plausible mechanism of the fast catalytic cycle on Co_3O_4 surfaces features in its initial phase a Co^{III}(OH)–O–Co^{III}OH moiety converted by two sequentially arriving holes to the Co^{IV}(═O)–O–Co^{IV}═O intermediate accompanied by deprotonation. This site is expected to undergo facile spontaneous (dark) nucleophilic attack by H_2O to form the O–O bond of a hydroperoxide surface species, as shown in the mechanistic scheme of Fig. 21. Because Co^{IV} and Co^{III} are both low spin and pseudooctahedral, the O–O bond forming step is spin-allowed and essentially preserves the coordination geometry. Additional favorable factors are the absence of water deprotonation and the extra oxidation power available from adjacent, electronically coupled Co^{IV} centers. Co^{IV}(═O)–O–Co^{IV}═O moieties were found to be sites with the highest TOF at moderate overpotential in a recent DFT study of water oxidation on Co_3O_4 crystal surfaces by Plaisance and van Santen that included for the first time calculation of activation barriers.[178] The reaction at the Co^{IV}(═O)–O–Co^{IV}═O site involves nucleophilic attack by a water molecule as proposed in our mechanism although preferentially on the bridging O rather than a terminal oxo as shown in Fig. 21. The subsequent arrival of another hole leads to the formation of the observed superoxide intermediate absorbing at 1013 cm^{-1}. Elimination of O_2 requires an additional hole, opening a coordination site for a H_2O molecule to regenerate the Co^{III}–OH center.

By contrast, for Co^{III}–OH sites on the Co_3O_4 surface that may lack an adjacent Co^{III}–OH group (illustrated by the Co^{III}OH site in the left corner of the Co_3O_4(111) facet depicted in the cartoon of Fig. 21B), the Co^{IV}═O intermediate generated upon hole transfer is unable to couple to another Co^{IV}═O. Nucleophilic

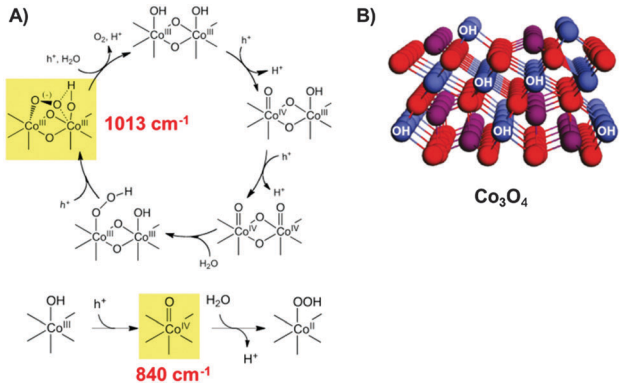

Fig. 21 Proposed reaction mechanism of water oxidation on the Co_3O_4 surface. (A) Mechanism of the fast site (top) and the slow site (bottom). Reproduced from ref. 168 with permission from the Nature Publishing Group. (B) Partially OH terminated $Co_3O_4(111)$ surface illustrates the octahedral Co^{III}–OH surface centers with and without adjacent Co^{III}–OH groups. Co^{III}: blue; Co^{II}: purple; O: red.

attack of an H_2O molecule on such isolated oxo Co^{IV} groups faces barriers not present for the $Co^{IV}(=O)$–O–$Co^{IV}=O$ sites, especially reduction to Co^{II} that likely requires spin flip and substantial coordination geometry changes, in addition to the need for the deprotonation of H_2O and the absence of additional oxidation power of an adjacent Co^{IV} center. Hence, the O–O bond forming step of an isolated Co site is expected to be a slow spontaneous reaction, and we attribute the 840 cm^{-1} species and its slow decay of 1 s^{-1} to this site (Fig. 20). In the recent theoretical work, isolated Co surface centers were calculated to exhibit high TOF only under large overpotential conditions especially on the (001) facet of Co_3O_4 although this was calculated for a highly oxidized Co^{V} surface center.[178]

The fast site with a TOF of approx. 3 s^{-1} discovered by the time-resolved FT-IR study exceeds the average value of 0.02 s^{-1} derived from steady state measurements by over 2 orders of magnitude. Hence, our study reveals that even for single crystal Co_3O_4 nanoparticles, surface sites with widely different catalytic activities exist. The structural origin of the activity differences is attributed to the ability (or lack) of an oxo Co^{IV} site to couple *via* the O bridge to another $Co^{IV}=O$ group. Such $Co^{IV}(=O)$–O–$Co^{IV}=O$ intermediates might not originate from a static set of $Co^{III}(OH)$–O–$Co^{III}OH$ sites on the crystal surface, however. The remarkably long period for the formation of partially oxidized $^{18}O^{16}O$ superoxide surface intermediates for experiments with parent catalyst $Co_3{}^{16}O_4$ in pure $H_2{}^{18}O$ (the change of the ratio of partially labeled $^{18}O^{16}O$ to fully labeled $^{18}O^{18}O$ superoxide from 1 : 1 to 1 : 8 requires a photolysis period of 1500 ms, and partially labeled $^{18}O^{16}O$ gas is observed even after 20 min (Fig. 18Ab and 19B)) points to a large reservoir of fast catalytic sites formed randomly on the surface in a dynamic process. We propose that each sequential hole injected into a Co_3O_4 particle generates a $Co^{IV}=O$ site at a random location on the surface because octahedral Co^{III}–OH groups are by far the most abundant surface sites on any Co_3O_4 nanoparticle by orders of magnitude even at maximum catalytic activity. Therefore, this is the most probable, and only, step of the entire catalytic cycle directly initiated by charge transfer from the visible light sensitizer. Random surface hole hopping through fast, proton coupled exchange of the type

$$Co^{IV}(=O)\text{–}O\text{–}Co^{III}\text{–}OH \rightarrow Co^{III}(OH)\text{–}O\text{–}Co^{IV}=O$$

results in the formation of $Co^{IV}(=O)$–O–$Co^{IV}=O$ intermediates at any location on the crystal surface that is part of a contiguous network of neighboring Co^{III}–OH sites, which may or may not involve Co centers that participated in a previous catalytic event. In this way, the entire network of adjacent Co^{III}–OH sites on the particle surface constitutes a pool of sites able to react with H_2O to form a surface hydroperoxide intermediate. Rate and spatial reach of surface hole hopping may significantly affect the water oxidation activity of a given Co oxide catalyst. Therefore, differences in surface OH termination of various Co oxide catalysts may influence catalytic activity by virtue of the dynamics by which sequential charges drive catalytic cycles, in addition to energetics and activation barriers of surface intermediates formed along the catalytic path.

4.3 Mechanism of electrochemically driven Co oxide catalysts

The main feature of the proposed water oxidation mechanism of the fast site, which is the formation of the $Co^{IV}(=O)$–O–$Co^{IV}=O$ moiety (with pronounced oxyl electronic character of the CoO groups),[171] has commonality with the reaction path proposed for amorphous Co oxide electrodeposits like Co–Pi.[161,171,176,179] For this electrocatalyst, $Co^{IV}=O$ was detected *ex situ* by low temperature EPR spectroscopy,[180] while *in situ* X-ray absorption spectroscopy under applied potential confirmed that the average Co oxidation state rises above Co^{III}, as shown in Fig. 22.[181] Also, a distinct XAS pre-edge peak of Co^{IV} was observed by high energy resolution fluorescence detection of a Co oxy hydroxide structural phase on the Au(111) substrate under O_2 evolution conditions.[182] Transient monitoring of water oxidation using surface interrogation scanning electrochemical microscopy (time resolution 10 ms) which allows selective titration of Co^{IV} centers revealed a reaction rate constant of >2 s^{-1} (TOF = 3.2 s^{-1} per surface Co^{IV}),[183,184] which is the same as the TOF of the fast catalytic site of Co_3O_4 determined by rapid-scan FT-IR measurements discussed above.[168]

It is not known at present whether similarities between the water oxidation mechanism on Co_3O_4 and Co–Pi or other amorphous Co oxide electrocatalysts extend further, in part because the starting point for Co–Pi electrocatalysis is Co^{II},[161,171,176,179,185,186] whereas for Co_3O_4 experimental evidence shows that the starting points for water oxidation catalysis are octahedral Co^{III} centers; tetrahedral Co^{II} centers of the spinel structure do not participate in the catalytic cycle. A particularly interesting question is whether O–O bond formation in the case of amorphous Co oxide electrocatalysts occurs by the nucleophilic attack of H_2O on a $Co^{IV}(=O)$–O–$Co^{IV}=O$ site to give the hydroperoxide intermediate as is the case for Co_3O_4, or whether the O–O bond emerges from coupling of adjacent $Co^{IV}=O$ surface sites. The latter mechanism was inferred from ^{18}O labelling isotope-ratio membrane inlet mass spectroscopy for the case of amorphous Co oxide nanoparticles prepared by oxidation of Co^{2+} in the presence

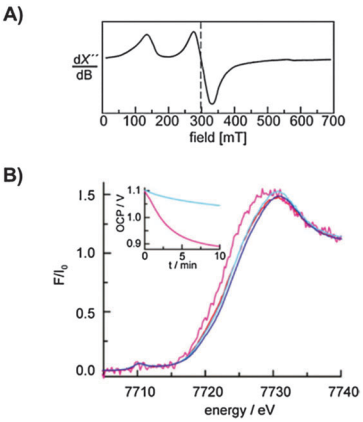

Fig. 22 Detection of Co^{IV} sites of the electrodeposited Co–Pi catalytic film for water oxidation. (A) EPR signal (4 degree K) of Co^{IV} measured *ex situ* after the oxygen evolution experiment. Reproduced from ref. 180 with permission from the American Chemical Society. (B) *In situ* X-ray absorption spectra of the Co–Pi film recorded *in situ* during electrocatalytic for water oxidation. Open circuit potential (magenta), 1.25 V (red). As reference, bulk Co oxide films at open circuit potential (cyan) and 1.25 V (blue) are shown. The inset shows the open circuit potential as a function of time. Reproduced from ref. 181 with permission from the American Chemical Society.

of methylenediphosphonic acid.[187] Direct observation of elementary catalytic steps on the surface of Co oxide electrocatalysts under operating conditions using structure specific vibrational spectroscopy would add important insights, but it awaits the development of appropriate triggering methods for time resolved monitoring under applied electrical bias.

Possibly the most important performance differences among various Co oxide catalysts are differences in the bulk and/or surface structure that give rise to different pathways and rates at which sequential charges driving the water oxidation cycle are delivered to the catalytic sites. Co^{IV} mobility resulting in encounters that lead to O–O bond formation has been recognized as a critical factor of efficient water oxidation in electrochemically driven Co oxide deposits as well.[161,188,189] The probability of such encounters is expected to be very sensitive to the specific patterns by which adjacent octahedral Co–OH sites are arranged on the surface as mentioned above, as well as other molecular level details of the catalyst surface. Regarding charge delivery through the bulk, a spectroscopically well supported case of how motifs can enhance O_2 evolution activity is delithiated $LiCoO_2$ (spinel or layered type) in which 3-dimensional Co–O–Co networks provide efficient hole transport pathways not available in the catalytically much less active structure prior to the removal of Li.[190] In this context, it is important to point out that the electrical bias applied during electrocatalytic O_2 evolution alters the geometrical structure of Co oxide catalysts according to the Pourbaix diagram, which typically results in an oxyhydroxide (layered double hydroxide) structure.[191–195] As mentioned in Section 4.2, such electrical bias-induced restructuring is absent in photosensitized catalysis over short periods of time, *e.g.* in transient spectroscopic studies where a single light pulse of millisecond duration or shorter is employed per sample for elucidating mechanisms. It is to be expected that for metal oxide surfaces where multiple catalytic pathways for water oxidation are accessible, the dominant pathway might change depending on operating conditions. For example, increase or decrease of the rate at which charges are delivered to the catalytic sites, which is controlled by the applied potential (electrochemical) or light intensity (photochemical), might alter the relative rate at which different catalytic sites receive, and are activated, by charge.

5. Assembly for closing of the photosynthetic cycle on the nanoscale under product separation

The availability of Co_3O_4 nanoparticles with nanotube morphology as water oxidation catalysts opens up the development of an integrated photosystem for CO_2 reduction by H_2O that accomplishes the complete catalytic cycle on the nanoscale under membrane separation. At the same time the system extends the product separation to the macroscale, as shown in the cartoon of Fig. 23. In this core–shell nanotube array, each nanotube functions as an independent photosynthetic unit. The inside of the tube and the surrounding environment (both ends of the nanotube are open) contain a vapor mixture of H_2O and O_2 in the form of moist air, with water oxidation taking place on the inner surface of the Co_3O_4 nanotube. CO_2 is loaded into the space between the separated core–shell nanotubes where photoreduction to fuel occurs. The spaces for CO_2 reduction and water oxidation and the fluids they contain are separated once sheets at the top and bottom are installed (Fig. 23, featuring openings on the tube ends). This core–shell nanotube array design addresses several major challenges of artificial photosystems: minimizing ohmic resistance losses inherent to ion transport over macroscale distances, avoiding large amounts of electrolyte, blocking cross-over of redox products, and offering vapor phase operation which bypasses low CO_2 solubility in liquid water. Meeting these challenges is essential for scalability of artificial photosystems on an appropriate scale (terawatts) for practical impacts on replacing fossil by solar transportation fuels.

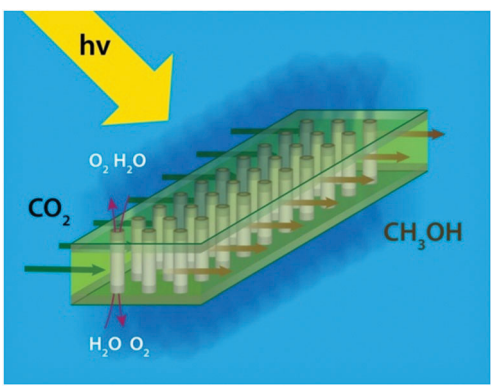

Fig. 23 Co_3O_4–SiO_2 core–shell nanotube array design for artificial photosynthesis.

Key requirements for the nanoscale membrane that separates the water oxidation catalysis on the inside of the Co_3O_4 nanotube from the light absorber and the CO_2 reduction sites on the outside are the complete blocking of O_2 and other small molecules from crossing while providing adequate transport of protons from the water oxidation side to the opposing side. Particularly important is efficient, tightly controlled transfer of charges (holes) across the membrane. Our concept is to use nanometer thick dense phase silica as a proton conducting membrane[196,197] with embedded molecular wires for charge transport, as illustrated in the cartoon Fig. 24A. The electronic properties of embedded molecular wires are selected for efficient hole transport from the light absorbed donor metal to the Co_3O_4 catalyst while blocking transfer of the excited electron on the light absorber acceptor metal to Co_3O_4. *P*-Oligo(phenylenevinylene) molecules, specifically the one featuring 3 aryl units (1,3-di((*E*)-styryl)benzene, abbreviated PV3), possess HOMO (1.4 V *vs.* NHE) and LUMO (−1.8 V) potentials[198] properly positioned between the redox potential of the excited ZrOCo unit (~1.7 V) and the HOMO of Co_3O_4 (1.2 V).[199] According to these potentials of the components, fast incoherent hopping of holes from the light absorber to the catalyst is expected while the transfer of the excited chromophore electron across the wire is minimized. That is, the appropriately positioned HOMO and LUMO of the molecular wire result in the rectifying behavior of the light absorber-wire assembly as shown in Fig. 24B, which prevents the loss of photocatalytic efficiency by misdirected electron transfer. Impermeability for O_2 of the silica protects the organic wire molecules from oxidative damage.[164]

5.1 Embedded molecular wires for controlled charge transport

In order to develop synthetic methods for casting organic molecular wires into silica and apply spectroscopic and electrochemical probes for detecting and quantifying charge transport across the membrane, we have used spherical Co_3O_4–SiO_2 core shell nanoparticles as well as cm^2 sized planar Co_3O_4–SiO_2 constructs.[166,200] For covalent anchoring of the 2 nm long PV3 molecules on Co_3O_4 surfaces, wire molecules were synthesized that feature a tripodal anchor on one end (the tridentate polyalcohol amide (1,3-dihydroxy-2-(hydroxymethyl)propan-2-yl)-carbamoyl) and one or two sulfonate groups on the other end (Fig. 24A).[201] The tripodal anchor is known to impose the vertical (radial) arrangement of organics on the oxide surface.[202] To enforce the radial arrangement, the opposite end of the wire molecule was functionalized by one or two sulfonate groups that are repelled by the negatively charged Co_3O_4 surface. For casting of the wire molecules into silica, we employed different methods for spherical and planar constructs. In the case of 4 nm Co_3O_4 particles, a modified solvothermal method originally reported by Stoeber was used.[166,203] The method gives uniform silica shells of 2 nm thickness around 4 nm Co_3O_4 particles both in the absence and the presence or molecular wires as shown in Fig. 25A and B. FT-Raman spectra, presented in Fig. 25C, confirm the integrity of the PV3 wire molecules after silica casting.[166]

Transient absorption spectroscopy revealed hole transfer from a visible light sensitizer, $[Ru(bpy(CO_2Me)_2)_3]^{2+}$, to Co_3O_4–PV_3–SiO_2 nanoparticles in aqueous suspension. As illustrated by the schematic of Fig. 26A, excitation of the MLCT transition of the sensitizer at 450 nm with an 8 ns laser pulse in the presence of electron acceptor $Co(NH_3)_5Cl_3$ formed $[Ru(bpy(CO_2Me)_2)_3]^{3+}$. Upon encounter of the oxidized sensitizer with a Co_3O_4–PV3–SiO_2 particle, a hole is injected into the particle as can be seen by the recovery of the MLCT bleach of $[Ru(bpy(CO_2Me)_2)_3]^{2+}$ with a time constant of 294 μs in Fig. 26B. The decay corresponds to a diffusion controlled rate of $k = 8 \times 10^{10}$ L mol^{-1} s^{-1}, indicating very efficient hole transfer to the embedded molecular wires. No hole injection was observed in the absence of embedded wires. The hole on the free wire molecule, or on the wire molecule anchored on silica has a spectral signature by an absorption band at 600 nm, shown in Fig. 26C.[201] When the PV3 wire molecules are anchored on Co_3O_4 as they are in Co_3O_4–PV3–SiO_2 particles, no 600 nm signal is detected (Fig. 26D). This is expected because of the efficient transfer of the hole to Co_3O_4. Silica on the other hand has no properly positioned acceptor state for the hole, and the charge remains on the wire molecule for hundreds of μs. The kinetic data of Fig. 26 allowed us to estimate an upper limit of at most a few microseconds for hole transfer from the embedded molecular wire to the Co_3O_4 catalyst.

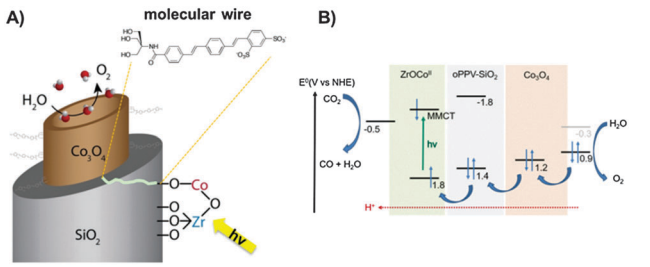

Fig. 24 Molecular wires for controlled charge transport embedded in the nanometer thick silica membrane. (A) Schematic of the Co_3O_4–SiO_2 core–shell nanotube with the ZrOCo light absorber coupled to *p*-oligo-(phenylenevinylene) wire cast into the silica shell. (B) Energetics of the HOMO and the LUMO of the light absorber, molecular wire, and catalyst. Adapted from ref. 164 with permission from the Royal Society of Chemistry.

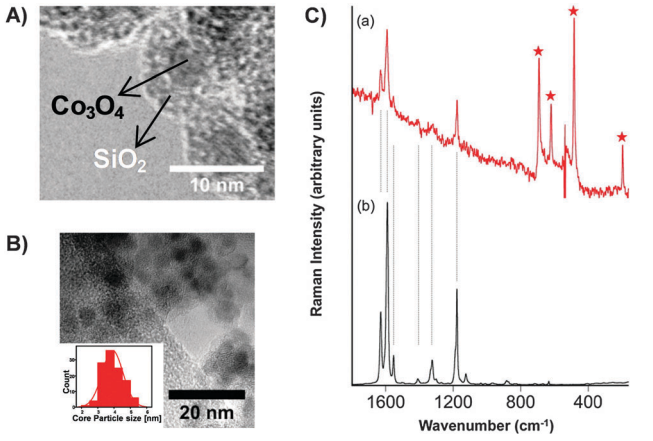

Fig. 25 Co_3O_4–SiO_2 core–shell nanoparticles (A) without and (B) with embedded PV3 wire molecules. (C) Trace (a): FT-Raman spectra of Co_3O_4–PV3–SiO_2 core–shell particles. Trace (b): free PV3 molecules (powder). From ref. 166, with permission.

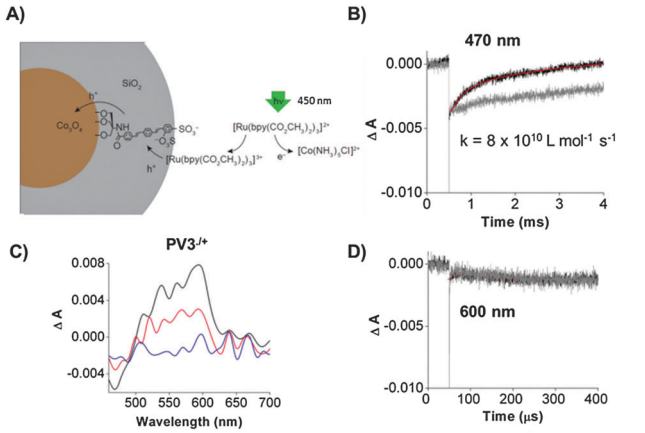

Fig. 26 Transient optical spectroscopy of hole transfer to silica embedded molecular wire. (A) Schematic of the visible light induced hole transfer process from the sensitizer on the outside to the Co_3O_4 particle on the inside of the core–shell particle. (B) Black trace: recovery of the bleach of the Ru sensitizer complex (470 nm) upon hole injection into embedded wire molecules. Grey trace: Co_3O_4–SiO_2 particles with no wires. (C) Transient absorption spectra of PV3 wire anchored on the silica surface (time slices at 40, 200, and 800 μs after hole injection). (D) Transient absorption measurement at 600 nm of the Co_3O_4–PV3–SiO_2 particle. Reproduced from ref. 166 and 201 with permission from the American Chemical Society.

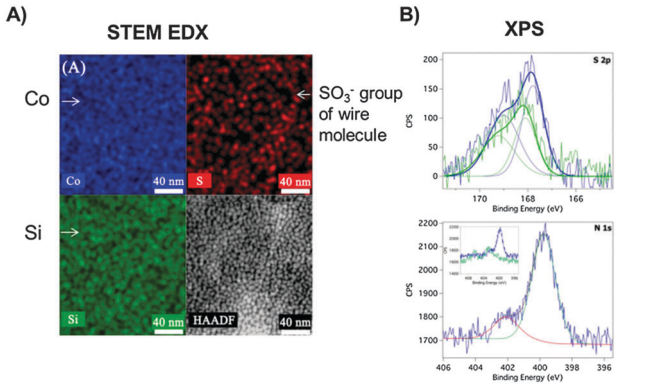

Fig. 27 Spectroscopic characterization of planar Co_3O_4–SiO_2 constructs with embedded PV3 wires. (A) EDX maps of Co, top left; Si, bottom left; S, top right; dark field image, bottom right. (B) XPS of the planar Co_3O_4–PV3 sample before (blue) and after deposition of 2.3 nm of silica (green). Sulfur S(2p) XPS of the SO_3^- substituent of wire molecules (top). Nitrogen N(1s) XPS of the amide group of wire (bottom). The small peak at 402 eV is due to the residual HTCU reagent. Smooth traces show spectral deconvolutions. Reproduced from ref. 200 with permission from the American Chemical Society.

Using the $[Ru(bpy)_3]^{2+}$ sensitizer, photo-electrochemical measurements of hole transfer through embedded PV3 in planar Co_3O_4–PV3–SiO_2 constructs allowed us to demonstrate that holes injected into the wire molecules are transferred to Co_3O_4, and to quantify the charge flow.[200] Square cm sized electrodes were prepared consisting of 100 nm Pt on crystalline Si covered by Co_3O_4 and anchored PV3 wires embedded in a 2 nm layer of SiO_2. The Co oxide and silica were deposited by mild temperature (plasma enhanced) atomic layer deposition (ALD) methods. As shown in the scanning transmission electron microscopy/energy dispersive X-ray images (STEM EDX) of Fig. 27A, ALD yields uniform Co_3O_4 layers onto which molecular wires anchor covalently in a well dispersed fashion. Subsequent ALD of tris-dimethylaminosilane precursor results in conformal silica coverage (2.3 nm thickness for the sample shown). The sulfur image in Fig. 27A originates from the sulfonate group of the anchored PV3 molecules after casting of silica. Analysis indicates an average loading of 1 wire molecule nm^{-2}, which corresponds to 0.2 monolayer coverage of the Co_3O_4 layer.[200] The presence of embedded wire molecules is confirmed by X-ray photoelectron spectroscopy (XPS) of S (originating from the sulfonate group) and N (amide linkage of tripod), as shown in Fig. 27B. Comparison of XPS spectra before (blue traces) and after (green) confirms that the wire molecules are preserved after casting of silica by the ALD method, and their structural integrity is further indicated by ATR FT-IR spectra recorded at a grazing angle.[200]

Electrochemical measurements of visible light induced charge injection into the Pt–Co_3O_4–PV_3–SiO_2 electrode in short circuit configuration as schematically described in Fig. 28A allowed us to determine charge flow across the membrane. The observed current upon 476 nm illumination of the $[Ru(bpy)_3]^{2+}$–persulfate system corresponded to 27 ± 3 electron per s^{-1} per molecular wire on average, which is substantially below the known capacity of electron flux for OPPV wires.[204] Therefore, charge transport across the nanoscale silica membrane will not be a rate limiting factor in an integrated system even at maximum solar intensity. No current was observed for Co_3O_4–SiO_2 electrodes without embedded molecular wires (Fig. 28B), or when a sensitizer was used with electronic properties that did not match the HOMO or LUMO energetics of PV3. For the latter experiment, Sn porphyrin (Sn(P)) was excited in the presence of the trimethylamine donor, which yields the Sn(P) radical anion that has insufficient potential to inject an electron into the LUMO of PV3.[205,206] Hence, the electronic properties of the embedded molecular wire tightly control charge transport across the silica membrane. Furthermore, the experiment confirms that the membrane is free of pinholes (photocurrent is observed when conducting the Sn(P) photosensitization with bare Co_3O_4).[200] The pinhole free nature of the SiO_2–PV3 membrane was further demonstrated by cyclic voltammetry (CV) scans using the ferrocene/ferrocenium couple as a probe. As shown in Fig. 28C, the ferrocene CV wave is readily observed for bare Co_3O_4 electrodes, but not when the Co oxide film is coated with the silica membrane with an embedded wire molecule. This is in agreement with the fact that the ferrocene redox potential is situated in the HOMO–LUMO gap of the wire molecule.

5.2 Proton conduction and gas blocking properties of the nanoscale silica membrane

In addition to controlled electron transport, the insulating silica membrane needs to transmit H^+ but block O_2 and other small molecules. Protons generated on the water oxidation side are needed on the reduction side for the formation of hydrocarbon fuel from CO_2, in addition to providing charge balance during operation. For characterizing proton transport and O_2

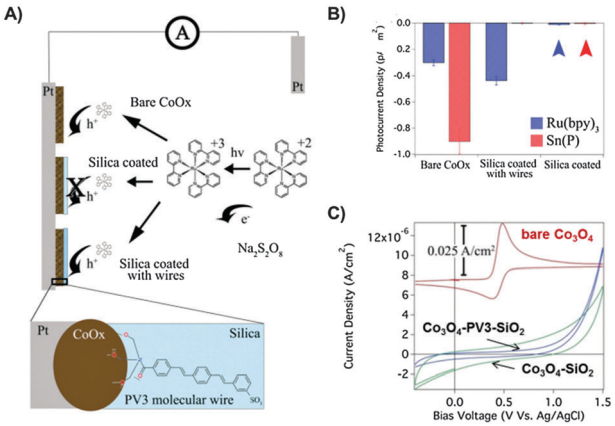

Fig. 28 Photoelectrochemical and CV measurements of charge transport across the silica membrane with embedded wires. (A) Schematic of visible light sensitized short circuit photocurrent measurements using $Ru(bpy)_3$–persulfate and Sn porphyrin (Sn(P))–triethylamine systems. (B) Photocurrent observed for hole injection into bare Co oxide, Co oxide coated with the SiO_2–PV3 membrane, and Co oxide coated with silica only. (C) CV of ferrocene (in acetonitrile containing 0.1 M *tert*-butylammonium perchlorate) using bare Co_3O_4 on the Pt electrode (red curve, offset for clarity), Co_3O_4–PV3–SiO_2 (blue curve), and Co_3O_4–SiO_2 (green curve). Reproduced from ref. 200 with permission from the American Chemical Society.

permeability by electrochemical measurements, we prepared Pt electrodes on the Si crystal onto which SiO_2 layers of precise thickness were grown by plasma-enhanced ALD. Fig. 29A shows a cross-sectional high resolution TEM image of a 3.8 ± 0.3 nm thick, extremely smooth silica layer on Pt (root-mean-square surface roughness 1.93 Å by AFM).[164] The construct was used as a working electrode in a 3-electrode cell depicted in Fig. 29B. Cathodic CV sweeps in pH 4 solution showed a peak at 0.23 V RHE, which is characteristic of the reduction of protons on the Pt surface that diffused through the silica layer, forming Pt–H. Analysis of the CV curve indicates a flux of 2.5 protons s^{-1} nm^{-2}

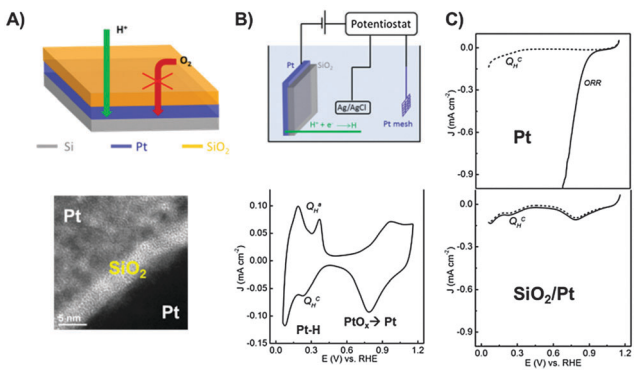

Fig. 29 Electrochemical measurement of the proton and oxygen permeability properties of nanoscale silica layers. (A) Cross-sectional high resolution TEM of the 3.8 nm SiO_2 layer deposited by ALD on the 100 nm Pt electrode, which was e-beam evaporated on the crystalline Si wafer. (B) Cyclic voltammetry of the SiO_2 coated Pt electrode (sample shown in A) at 298 K at pH 4 (0.5 M Na_2SO_4). The scan rate is 50 mV s^{-1}. (C) CV of air saturated aqueous solution of the bare Pt electrode (top) and the Pt electrode coated with the 3.8 nm SiO_2 layer (bottom). Adapted from ref. 164 with permission from the Royal Society of Chemistry.

which was sustained over several hours of continuous cycling (Fig. 29B, bottom). Phosphorous or transition metal doping of the silica during the ALD process can be used to enhance the proton flux if needed.[196,197] The same electrode was used to assess O_2 permeability. No O_2 reduction was observed for silica layer thickness above 2 nm when conducting the CV experiments in O_2 saturated solution (Fig. 29C).

With their proton conducting and O_2 blocking properties and tightly controlled charge transfer, the nanoscale silica layers with embedded molecular wires offer a novel membrane for nanoscale artificial photosystems.

6. Outlook

With silica layers with embedded molecular wires now at hand as nanoscale membranes for artificial photosynthesis, and Co_3O_4 nanoparticles found to be sufficiently efficient as water oxidation catalysts, integrated systems for visible light induced reduction of CO_2 by H_2O based on these materials can be explored. The mild temperature ALD method with its precise control of layer thickness for the preparation of catalyst nanostructures and nanoscale silica membranes with embedded wire molecules can be adapted to many different morphologies and therefore enables the hierarchical assembly of artificial photosystems in a variety of geometries. Macroscale arrays in the form of Co oxide–silica nanotubes offer one such arrangement for separating water oxidation catalysis from the light absorber and carbon dioxide reduction to fuel while closing the photocatalytic cycle on the nanoscale, and one can envision others. By using Earth abundant materials, scalable synthetic methods, and by focusing on robust inorganic oxide structures, the nanotube array approach provides opportunities for developing viable artificial photosystems for visible light CO_2 reduction by H_2O. The nanotube array geometry offers flexibility for maximizing photocatalytic efficiency by adjusting structural parameters such as nanotube size, their spacing, and electronic properties of molecular wires and light absorbers. The pursuit of a diversity of ideas for structures is needed to converge towards the most efficient integrated system for the direct solar light driven reduction of carbon dioxide by water.

Acknowledgements

This work was supported by the Director, Office of Science, Office of Basic Energy Sciences, Division of Chemical, Geological and Biosciences of the U.S. Department of Energy under Contract No. DE-AC02-05CH11231.

Notes and references

1 A. Modestino, K. A. Walczak, A. Berger, C. M. Evans, S. Haussener, C. Koval, J. S. Newman, J. W. Ager and R. A. Segalman, *Energy Environ. Sci.*, 2014, 7, 297–301.
2 E. A. Hernandez-Pagan, N. M. Vergas-Barbosa, T. H. Wang, Y. Zhao, E. S. Smotkin and T. E. Mallouk, *Energy Environ. Sci.*, 2012, 5, 7582–7589.

3 W. Lin and H. Frei, *J. Am. Chem. Soc.*, 2005, **127**, 1610–1611.
4 W. Lin and H. Frei, *J. Phys. Chem. B*, 2005, **109**, 4929–4935.
5 D. Zhao, J. Feng, Q. Huo, N. Melosh, G. H. Fredrickson, B. F. Chmelka and G. D. Stucky, *Science*, 1998, **279**, 548–552.
6 T. Maschmeyer, F. Rey, G. Sankar and J. M. Thomas, *Nature*, 1995, **378**, 159–162.
7 M. L. Macnaughtan, H. S. Soo and H. Frei, *J. Phys. Chem. C*, 2014, **118**, 7874–7885.
8 H. S. Soo, M. L. Macnaughtan, W. W. Weare, J. Yano and H. Frei, *J. Phys. Chem. C*, 2011, **115**, 24893–24905.
9 T. Cuk, W. W. Weare and H. Frei, *J. Phys. Chem. C*, 2010, **114**, 9167–9172.
10 H. Han and H. Frei, *J. Phys. Chem. C*, 2008, **112**, 8391–8399.
11 H. Han and H. Frei, *Microporous Mesoporous Mater.*, 2007, **103**, 265–272.
12 H. Han and H. Frei, *J. Phys. Chem. C*, 2008, **112**, 16156–16159.
13 R. Nakamura and H. Frei, *J. Am. Chem. Soc.*, 2006, **128**, 10668–10669.
14 R. Nakamura, A. Okamoto, H. Osawa, H. Irie and K. Hashimoto, *J. Am. Chem. Soc.*, 2007, **129**, 9596–9597.
15 A. Okamoto, R. Nakamura, H. Osawa and K. Hashimoto, *Langmuir*, 2008, **24**, 7011–7017.
16 X. Wu, W. W. Weare and H. Frei, *Dalton Trans.*, 2009, 10114–10121.
17 H. Frei, *Chimia*, 2009, **63**, 721–730.
18 B. A. McClure and H. Frei, *J. Phys. Chem. C*, 2014, **118**, 11601–11611.
19 G. Blasse, *Struct. Bonding*, 1991, **76**, 153–187.
20 D. M. Sherman, *Phys. Chem. Miner.*, 1987, **14**, 364–367.
21 D. M. Sherman, *Phys. Chem. Miner.*, 1987, **14**, 355–363.
22 R. G. Burns, D. A. Nolet, K. M. Parkin, C. A. McCammon and K. B. Schwartz, in *Mixed-Valence Compounds*, ed. D. B. Brown, 1980, pp. 295–336.
23 R. G. Burns, *Annu. Rev. Earth Planet. Sci.*, 1981, **9**, 345–383.
24 A. N. Platanov, K. Langer, S. S. Matsuk, M. N. Taran and X. Hu, *Eur. J. Mineral.*, 1991, **3**, 19–26.
25 K. Langer, A. N. Platonov, S. S. Matsyuk and M. Wildner, *Eur. J. Mineral.*, 2002, **14**, 1027–1032.
26 G. Blasse, *Comments Inorg. Chem.*, 1981, **1**, 245–256.
27 A. J. Falzone, J. Nguyen, W. W. Weare, R. D. Sommer and P. D. Boyle, *Chem. Commun.*, 2014, **50**, 2139–2141.
28 X. Wu, T. Huang, T. T. Lekich, R. D. Sommer and W. W. Weare, *Inorg. Chem.*, 2015, **54**, 5322–5328.
29 E. N. Glass, J. Fielden, A. L. Kaledin, D. G. Musaev, T. Lian and C. L. Hill, *Chem. – Eur. J.*, 2014, **20**, 4297–4307.
30 J. K. McCusker, K. N. Walda, R. C. Dunn, J. D. Simon, D. Magde and D. N. Hendrickson, *J. Am. Chem. Soc.*, 1992, **114**, 6919–6920.
31 J. E. Monat and J. K. McCusker, *J. Am. Chem. Soc.*, 2000, **122**, 4092–4097.
32 N. Huse, H. Cho, K. Hong, L. Jamula, F. M. F. De Groot, T. K. Kim, J. K. McCusker and R. W. Schoenlein, *J. Phys. Chem. Lett.*, 2011, **2**, 880–884.
33 Y.-J. Chen, J. F. Endicott and P. G. McNamarra, *J. Phys. Chem. B*, 2007, **111**, 6748–6760.
34 J. F. Endicott, Y.-J. Chen and P. Xie, *Coord. Chem. Rev.*, 2005, **249**, 343–373.
35 X. Song, Y. Lei, S. Van Wallendal, M. W. Perkovic, D. C. Jackman, J. F. Endicott and D. P. Rillema, *J. Phys. Chem.*, 1993, **97**, 3225–3236.
36 B. P. Macpherson, P. V. Bernhardt, A. Hauser, S. Pagès and E. Vauthey, *Inorg. Chem.*, 2005, **44**, 5530–5536.
37 O. Sato, T. Iyoda and A. Fujishima, *Science*, 1996, **272**, 704–705.
38 A. Bleuzen, C. Lomenech, A. Dolbecq, F. Villain, A. Goujon, O. Roubeau, M. Nogues, F. Varret, F. Baudelet, E. Dartyge, C. Giorgeti, J.-J. Gallet, C. C. D. Moulin and M. Verdaguer, *Mol. Cryst. Liq. Cryst.*, 1999, **335**, 253–262.
39 R. Le Bris, Y. Tsunobuchi, C. Mathoniere, H. Tokoro, S. Ohkoshi, N. Ould-Moussa, G. Molnar, A. Bousseksou and J.-F. Létard, *Inorg. Chem.*, 2012, **51**, 2852–2859.
40 R. Le Bris, C. Mathonière and J.-F. Létard, *Chem. Phys. Lett.*, 2006, **426**, 380–386.
41 S. Gawali-Salunke, F. Varret, I. Maurin, C. Enachescu, M. Malarova, K. Boukheddaden, E. Codjovi, H. Tokoro, S. Ohkoshi and K. Hashimoto, *J. Phys. Chem. B*, 2005, **109**, 8251–8256.
42 C. Chong, M. Itoi, K. Boukheddaden, E. Codjovi, A. Rotaru, F. Varret, F. A. Frye, D. R. Talham, I. Maurin, D. Chernyshov and M. Castro, *Phys. Rev. B: Condens. Matter Mater. Phys.*, 2011, **84**, 144102.
43 L. K. Anderson and H. Frei, *J. Phys. Chem. B*, 2006, **110**, 22601–22607.
44 Y. Hori, *Modern Aspects of Electrochemistry*, Springer, New York, 2008, vol. 42, pp. 89–189.
45 M. Gattrell, N. Gupta and A. Co, *J. Electroanal. Chem.*, 2006, **594**, 1–19.
46 K. J. P. Schouten, Y. Kwon, C. J. M. van der Ham, Z. Qin and M. T. M. Koper, *Chem. Sci.*, 2011, **2**, 1902–1909.
47 C. W. Li and M. W. Kanan, *J. Am. Chem. Soc.*, 2012, **134**, 7231–7234.
48 R. Reske, H. Mistry, F. Behafarid, B. Roldan Cuenya and P. Strasser, *J. Am. Chem. Soc.*, 2014, **136**, 6978–6986.
49 A. S. Varela, C. Schlaup, Z. P. Jovanov, P. Malacrida, S. Horch, I. E. L. Stephens and I. Chorkendorff, *J. Phys. Chem. C*, 2013, **117**, 20500–20508.
50 M. Le, M. Ren, Z. Zhang, P. T. Sprunger, R. L. Kurtz and J. C. Flake, *J. Electrochem. Soc.*, 2011, **158**, E45–E49.
51 S. Sen, D. Liu and G. T. R. Palmore, *ACS Catal.*, 2014, **4**, 3091–3095.
52 R. Reske, M. Duca, M. Oezaslan, K. J. P. Schouten, M. T. M. Koper and P. Strasser, *J. Phys. Chem. Lett.*, 2013, **4**, 2410–2413.
53 D. Kim, J. Resasco, Y. Yu, A. M. Asirl and P. Yang, *Nat. Commun.*, 2014, **5**, 4948.
54 S. Rasul, D. H. Anjum, A. Jedidi, Y. Minenkov, L. Cavallo and K. Takanabe, *Angew. Chem., Int. Ed.*, 2015, **54**, 2146–2150.
55 I. H. Tseng and J. C. S. Wu, *Catal. Today*, 2004, **97**, 113–119.
56 K. Tennakone, A. H. Jayatissa and S. Punchihewa, *J. Photochem. Photobiol., A*, 1989, **49**, 369–375.

57 W. Kim and H. Frei, *ACS Catal.*, 2015, **5**, 5627–5635.
58 B. Gholamkhass, H. Mametsuka, K. Koike, T. Tanabe, M. Furue and O. Ishitani, *Inorg. Chem.*, 2005, **44**, 2326–2336.
59 S. Sato, K. Koike, H. Inoue and O. Ishitani, *Photochem. Photobiol. Sci.*, 2007, **6**, 454–461.
60 K. Koike, S. Noito, S. Sato, Y. Tamaki and O. Ishitani, *J. Photochem. Photobiol., A*, 2009, **207**, 109–114.
61 E. Kato, H. Takeda, K. Koike, K. Ohkubo and O. Ishitani, *Chem. Sci.*, 2015, **6**, 3003–3012.
62 H. Takeda and O. Ishitani, *Coord. Chem. Rev.*, 2010, **254**, 346–354.
63 Z. Y. Bian, S. M. Chi and W. Fu, *Dalton Trans.*, 2010, **39**, 7884–7887.
64 Y. Tamaki, K. Watanabe, K. Koike, H. Inoue, T. Morimoto and O. Ishitani, *Faraday Discuss.*, 2012, **155**, 115–127.
65 Y. Tamaki, T. Morimoto, K. Koike and O. Ishitani, *Proc. Natl. Acad. Sci. U. S. A.*, 2012, **109**, 15673–15678.
66 F. Lakadamyali, A. Reynal, M. Kato, J. R. Durrant and E. Reisner, *Chem. – Eur. J.*, 2012, **18**, 15464–15475.
67 J. Willkomm, K. L. Orchard, A. Reynal, E. Pastor, J. R. Durrant and E. Reisner, *Chem. Soc. Rev.*, 2016, **45**, 9–23.
68 T. W. Woolerton, S. Sheard, E. Reisner, E. Pierce, S. W. Ragsdale and F. A. Armstrong, *J. Am. Chem. Soc.*, 2010, **132**, 2132–2133.
69 T. W. Woolerton, S. Sheard, E. Pierce, S. W. Ragsdale and F. A. Armstrong, *Energy Environ. Sci.*, 2011, **4**, 2393–2399.
70 C. D. Windle and R. N. Perutz, *Coord. Chem. Rev.*, 2012, **256**, 2562–2570.
71 E. G. Ha, J. A. Chang, S. M. Byun, C. Pac, D. M. Jang, J. Park and S. O. Kang, *Chem. Commun.*, 2014, **50**, 4462–4464.
72 T. Nakagawa, C. A. Beasley and R. W. Murray, *J. Phys. Chem. C*, 2009, **113**, 12958–12961.
73 T. Nakagawa, N. S. Bjorge and R. W. Murray, *J. Am. Chem. Soc.*, 2009, **131**, 15578–15579.
74 R. D. L. Smith, B. Sporinova, R. D. Fagan, S. Trudel and C. P. Berlinguette, *Chem. Mater.*, 2014, **26**, 1654–1659.
75 W. Kim, G. Yuan, B. A. McClure and H. Frei, *J. Am. Chem. Soc.*, 2014, **136**, 11034–11042.
76 N. Sivasankar, W. W. Weare and H. Frei, *J. Am. Chem. Soc.*, 2011, **133**, 12976–12979.
77 H. G. Sanchez-Casalongue, M. L. Ng, S. Kaya, D. Friebel, H. Ogasawara and A. Nilsson, *Angew. Chem., Int. Ed.*, 2014, **53**, 7169–7172.
78 J. Rossmeisl, Z. W. Qu, H. Zhu, G. J. Kroes and J. K. Norskov, *J. Electroanal. Chem.*, 2007, **607**, 83–89.
79 J. D. Blakemore, N. D. Schley, D. Balcells, J. F. Hull, G. W. Olack, C. D. Incarvito, O. Eisenstein, G. W. Brudvig and R. H. Grabtree, *J. Am. Chem. Soc.*, 2010, **132**, 16017–16029.
80 J. D. Blakemore, R. H. Crabtree and G. W. Brudvig, *Chem. Rev.*, 2015, **115**, 12974–13005.
81 N. Ulagappan and H. Frei, *J. Phys. Chem. A*, 2000, **104**, 7834–7839.
82 W. Lin, H. Han and H. Frei, *J. Phys. Chem. B*, 2004, **108**, 18269–18273.
83 R. E. Rocheleau, E. L. Miller and A. Misra, *Energy Fuels*, 1998, **12**, 3–10.
84 S. Y. Reece, J. A. Hamel, K. Sung, T. D. Jarvi, A. J. Esswein, J. J. H. Pijpers and D. G. Nocera, *Science*, 2011, **334**, 645–648.
85 O. Khaselev and J. A. Turner, *Science*, 1998, **280**, 425–427.
86 E. Verlage, S. Hu, R. Liu, R. J. R. Jones, K. Sun, C. Xiang, N. S. Lewis and H. A. Atwater, *Energy Environ. Sci.*, 2015, **8**, 3166–3172.
87 J. Brillet, J. H. Yum, M. Cornuz, T. Hisatomi, R. Solarska, J. Augustynski, M. Gratzel and K. Sivula, *Nat. Photonics*, 2012, **6**, 824–828.
88 F. F. Abdi, L. Han, A. H. M. Smets, M. Zeman, B. Dam and R. van de Krol, *Nat. Commun.*, 2013, **4**, 2195.
89 C. Liu, J. Tang, H. M. Chen, B. Liu and P. Yang, *Nano Lett.*, 2013, **13**, 2989–2992.
90 B. Liu, C. H. Wu, J. Miao and P. Yang, *ACS Nano*, 2014, **8**, 11739–11744.
91 M. R. Shaner, K. T. Fountaine, S. Ardo, R. H. Coridan, H. A. Atwater and N. Lewis, *Energy Environ. Sci.*, 2014, **7**, 779–790.
92 J. W. Jang, C. Du, Y. Ye, Y. Lin, X. Yao, J. Thorne, E. Liu, G. McMahon, J. Zhu, A. Javey, J. Guo and D. Wang, *Nat. Commun.*, 2015, **6**, 7447.
93 J. Luo, J. H. Im, M. T. Mayer, M. Schreier, M. K. Nazeeruddin, N. G. Park, S. D. Tilley, H. J. Fan and M. Graetzel, *Science*, 2014, **345**, 1593–1596.
94 K. Maeda, K. Teramura, D. Lu, T. Takata, N. Saito, Y. Inoue and K. Domen, *Nature*, 2006, **440**, 295.
95 Y. Sasaki, H. Nemoto, K. Saito and A. Kudo, *J. Phys. Chem. C*, 2009, **113**, 17536–17542.
96 T. Hisatomi, J. Kubota and K. Domen, *Chem. Soc. Rev.*, 2014, **43**, 7520–7535.
97 P. Zhou, J. Yu and M. Jaroniec, *Adv. Mater.*, 2014, **26**, 4920–4935.
98 K. Iwashina, A. Iwase, Y. H. Ng, R. Amal and A. Kudo, *J. Am. Chem. Soc.*, 2015, **137**, 604–607.
99 Y. Kim, D. Shin, W. J. Chang, H. L. Jang, C. W. Lee, H.-E. Lee and K. T. Nam, *Adv. Funct. Mater.*, 2015, **25**, 2369–2377.
100 J. C. Hemminger, R. Carr and G. A. Somorjai, *Chem. Phys. Lett.*, 1978, **57**, 100–104.
101 T. Inoue, A. Fujishima, S. Konishi and K. Honda, *Nature*, 1979, **277**, 637–638.
102 K. Sayama and H. Arakawa, *J. Phys. Chem.*, 1993, **97**, 531–533.
103 K. Iizuka, T. Wato, Y. Miseki, K. Saito and A. Kudo, *J. Am. Chem. Soc.*, 2011, **133**, 20863–20868.
104 M. S. Hamdy, R. Amrollahi, I. Sinev, B. Mei and G. Mul, *J. Am. Chem. Soc.*, 2014, **136**, 594–597.
105 A. Dhakshinamoorthy, S. Navalon, A. Corma and H. Garcia, *Energy Environ. Sci.*, 2012, **5**, 9217–9233.
106 W. Kim, T. Seok and W. Choi, *Energy Environ. Sci.*, 2012, **5**, 6066–6070.
107 S. Xie, Y. Wang, Q. Zhang, W. Deng and Y. Wang, *ACS Catal.*, 2014, **4**, 3644–3653.
108 T. Arai, S. Sato, T. Kajino and T. Morikawa, *Energy Environ. Sci.*, 2013, **6**, 1274–1282.

109 T. Arai, S. Sato and T. Morikawa, *Energy Environ. Sci.*, 2015, **8**, 1998–2002.
110 M. Schreier, L. Curvat, F. Giordano, L. Steier, A. Abate, S. M. Zakeeruddin, J. Luo, M. T. Mayer and M. Graetzel, *Nat. Commun.*, 2015, **6**, 7326.
111 M. Anpo and M. Takeuchi, *J. Catal.*, 2003, **216**, 505–516.
112 J. R. Swierk and T. E. Mallouk, *Chem. Soc. Rev.*, 2013, **42**, 2357–2387.
113 D. L. Ashford, M. K. Gish, A. K. Vannucci, M. K. Brennaman, J. L. Templeton, J. M. Papanikolas and T. J. Meyer, *Chem. Rev.*, 2015, **115**, 13006–13049.
114 L. Duan, L. Tong, Y. Xu and L. Sun, *Energy Environ. Sci.*, 2011, **4**, 3296–3313.
115 J. Ronge, T. Bosserez, D. Martel, C. Nervi, L. Boarino, F. Taulelle, G. Decher, S. Bordiga and J. A. Martens, *Chem. Soc. Rev.*, 2014, **43**, 7963–7981.
116 J. Yano, J. Kern, K. Sauer, M. J. Latimer, Y. Pushkar, J. Biesiadka, B. Loll, W. Saenger, J. Messinger, A. Zouni and V. K. Yachandra, *Science*, 2006, **314**, 821–825.
117 Y. Zhao, J. R. Swierk, J. D. Megiatto, B. Sherman, W. J. Youngblood, D. Qin, D. M. Lentz, T. A. Moore, D. Gust and T. E. Mallouk, *Proc. Natl. Acad. Sci. U. S. A.*, 2012, **109**, 15612–15616.
118 J. D. Megiatto, A. Antoniu-Pablant, B. D. Sherman, G. Kodis, M. Gervaldo, T. A. Moore, A. L. Moore and D. Gust, *Proc. Natl. Acad. Sci. U. S. A.*, 2012, **109**, 15578–15583.
119 J. R. Swierk, N. S. McCool and T. E. Mallouk, *J. Phys. Chem. C*, 2015, **119**, 13858–13867.
120 J. D. Megiatto, D. D. Mendez-Hernandez, M. E. Tejeda-Ferrari, A. L. Teillout, M. J. Llansola-Portoles, G. Kodis, O. G. Poluektov, T. Rajh, V. Mujica, T. L. Groy, D. Gust, T. A. Moore and A. L. Moore, *Nat. Chem.*, 2014, **6**, 423–428.
121 L. Hammarstroem and S. Styring, *Energy Environ. Sci.*, 2011, **4**, 2379–2388.
122 A. Magnuson, M. Anderlund, O. Johansson, P. Lindblad, R. Lomoth, T. Polivka, S. Ott, K. Stensjoe, S. Styring, V. Sundstroem and L. Hammarstroem, *Acc. Chem. Res.*, 2009, **42**, 1899–1909.
123 L. Li, L. Duan, Y. Xu, M. Gorlov, A. Hagfeldt and L. Sun, *Chem. Commun.*, 2010, **46**, 7307–7309.
124 G. F. Moore, J. D. Blakemore, R. L. Milot, J. F. Hull, H. Song, L. Cai, C. A. Schmuttenmaer, R. H. Crabtree and G. W. Brudvig, *Energy Environ. Sci.*, 2011, **4**, 2389–2392.
125 X. Xiang, J. Fielden, W. Rodriguez-Cordoba, Z. Huang, N. Zhang, Z. Luo, D. G. Musaev, T. Lian and C. L. Hill, *J. Phys. Chem. C*, 2013, **117**, 918–926.
126 M. Orlandi, R. Argazzi, A. Sartorel, M. Carraro, G. Scorrano, M. Bonchio and F. Scandola, *Chem. Commun.*, 2010, **46**, 3152–3154.
127 M. R. Norris, J. J. Concepcion, D. P. Harrison, R. A. Binstead, D. L. Ashford, Z. Fang, J. L. Templeton and T. J. Meyer, *J. Am. Chem. Soc.*, 2013, **135**, 2080–2083.
128 M. T. Vagnini, A. L. Smeigh, J. D. Blakemore, S. W. Eaton, N. D. Schley, F. D'Souza, R. H. Crabtree, G. W. Brudvig, D. T. Dick and M. R. Wasielewski, *Proc. Natl. Acad. Sci. U. S. A.*, 2012, **109**, 15651–15656.
129 N. N. Greenwood and A. Earnshaw, *Chemistry of the Elements*, Butterworth-Heinemann, Oxford, 2nd edn, 1997, p. 1113.
130 S. Trasatti, *Electrochim. Acta*, 1984, **29**, 1503–1512.
131 M. S. El-Deab, M. I. Awad, A. M. Mohammad and T. Ohsaka, *Electrochem. Commun.*, 2007, **9**, 2082–2087.
132 Y. Matsumoto and E. Sato, *Mater. Chem. Phys.*, 1986, **14**, 397–426.
133 C. Iwakura, A. Honji and H. Tamura, *Electrochim. Acta*, 1981, **26**, 1319–1326.
134 P. Rasiyah and A. C. C. Tseung, *J. Electrochem. Soc.*, 1983, **130**, 365–368.
135 R. N. Singh, D. Mishra, M. Anindita, A. S. K. Shinha and A. Singh, *Electrochem. Commun.*, 2007, **9**, 1369–1373.
136 T. Schmidt and H. Wendt, *Electrochim. Acta*, 1994, **39**, 1763–1767.
137 M. Morita, C. Iwakura and H. Tamura, *Electrochim. Acta*, 1978, **23**, 331–335.
138 M. Morita, C. Iwakura and H. Tamura, *Electrochim. Acta*, 1979, **24**, 357–362.
139 R. Mraz, V. Srb and S. Tichy, *Electrochim. Acta*, 1973, **18**, 551–554.
140 Y. Matsumoto and E. Sato, *Electrochim. Acta*, 1979, **24**, 421–423.
141 K. Fujimura, T. Matsui, K. Izumiya, N. Kumagai, E. Akiyama, H. Habazaki, K. Kawashima, K. Asami and K. Hashimoto, *Mater. Sci. Eng., A*, 1999, **267**, 254–259.
142 M. Morita, C. Iwakura and H. Tamaru, *Electrochim. Acta*, 1977, **22**, 325–328.
143 Y. Okuno, O. Yonemitsu and Y. Chiba, *Chem. Lett.*, 1983, 815–818.
144 V. Y. Shafirovich, N. K. Khannanov and A. E. Shilov, *J. Inorg. Biochem.*, 1981, **15**, 113–129.
145 A. Harriman, I. J. Pickering, J. M. Thomas and P. A. Christensen, *J. Chem. Soc., Faraday Trans. 1*, 1988, **84**, 2795–2806.
146 F. Jiao and H. Frei, *Angew. Chem., Int. Ed.*, 2009, **48**, 1841–1844.
147 F. Jiao and H. Frei, *Energy Environ. Sci.*, 2010, **3**, 1018–1027.
148 F. Jiao and H. Frei, *Chem. Commun.*, 2010, **46**, 2920–2922.
149 M. Zhang and H. Frei, *Catal. Lett.*, 2015, **145**, 420–435.
150 T. Kuwabara, E. Tomita, S. Sakita, D. Hasegawa, K. Sone and M. Yagi, *J. Phys. Chem. C*, 2008, **112**, 3774–3779.
151 M. Grzelczak, J. Zhang, J. Pfrommer, J. Hartmann, M. Driess, M. Antonietti and X. Wang, *ACS Catal.*, 2013, **3**, 383–388.
152 S. Yusuf and F. Jiao, *ACS Catal.*, 2012, **2**, 2753–2760.
153 V. B. R. Boppana and F. Jiao, *Chem. Commun.*, 2011, **47**, 8973–8975.
154 A. J. Esswein, M. J. McMurdo, P. N. Ross, A. T. Bell and T. D. Tilley, *J. Phys. Chem. C*, 2009, **113**, 15068–15072.
155 J. D. Blakemore, H. B. Gray, J. R. Winkler and A. M. Mueller, *ACS Catal.*, 2013, **3**, 2497–2500.
156 G. S. Hutchings, Y. Zhang, J. Li, B. T. Yonemoto, X. Zhou, K. Zhu and F. Jiao, *J. Am. Chem. Soc.*, 2015, **137**, 4223–4229.
157 P. W. Menezes, A. Indra, D. Gonzalez-Flores, N. R. Saharaie, I. Zaharieva, M. Schwarze, P. Strasser, H. Dau and M. Driess, *ACS Catal.*, 2015, **5**, 2017–2027.

158 H. Tuysuz, Y. J. Hwang, S. B. Khan, A. M. Asiri and P. Yang, *Nano Res.*, 2013, **6**, 47–54.
159 Y. J. Sa, K. Kwon, J. Y. Cheon, F. Kleitz and S. H. Joo, *J. Mater. Chem. A*, 2013, **1**, 9992–10001.
160 M. W. Kanan and D. G. Nocera, *Science*, 2008, **231**, 1072–1075.
161 D. G. Nocera, *Acc. Chem. Res.*, 2012, **45**, 767–776.
162 Y. Gorlin and T. F. Jaramillo, *J. Am. Chem. Soc.*, 2010, **132**, 13612–13614.
163 L. H. Zhuo, J. C. Ge, L. H. Cao and B. Tang, *Cryst. Growth Des.*, 2009, **9**, 1–6.
164 G. Yuan, A. Agiral, N. Pellet, W. Kim and H. Frei, *Faraday Discuss.*, 2014, **176**, 233–249.
165 N. D. Morris and T. E. Mallouk, *J. Am. Chem. Soc.*, 2002, **124**, 11114–11121.
166 A. Agiral, H. S. Soo and H. Frei, *Chem. Mater.*, 2013, **25**, 2264–2273.
167 S. Helveg, C. F. Kisielowski, J. R. Jinschek, P. Specht, G. Yuan and H. Frei, *Micron*, 2014, **68**, 176–185.
168 M. Zhang, M. de Respinis and H. Frei, *Nat. Chem.*, 2014, **6**, 362–367.
169 A. Zecchina, G. Spoto and S. Coluccia, *J. Mol. Catal.*, 1982, **14**, 351–355.
170 J. R. Winkler and H. B. Gray, *Struct. Bonding*, 2012, **142**, 17–28.
171 A. M. Ullman and D. G. Nocera, *J. Am. Chem. Soc.*, 2013, **135**, 15053–15061.
172 J. B. Gerken, J. G. McAlpin, J. Y. C. Chen, M. L. Rigsby, W. H. Casey, R. D. Britt and S. S. Stahl, *J. Am. Chem. Soc.*, 2011, **133**, 14431–14442.
173 X. L. Xu, Z. H. Chen, Y. Li, W. K. Chen and J. Q. Li, *Surf. Sci.*, 2009, **603**, 653–658.
174 J. Chen and A. Selloni, *J. Phys. Chem. Lett.*, 2012, **3**, 2808–2814.
175 A. Bergmann, E. Martinez-Moreno, D. Teschner, P. Chernev, M. Gliech, J. Ferreira de Araujo, T. Reier, H. Dau and P. Strasser, *Nat. Commun.*, 2015, **6**, 8625.
176 Y. Surendranath, M. W. Kanan and D. G. Nocera, *J. Am. Chem. Soc.*, 2010, **132**, 16501–16509.
177 L. P. Wang and T. Van Voorhis, *J. Phys. Chem. Lett.*, 2011, **2**, 2200–2204.
178 C. P. Plaisance and R. A. van Santen, *J. Am. Chem. Soc.*, 2015, **137**, 14660–14672.
179 M. W. Kanan, Y. Surendranath and D. G. Nocera, *Chem. Soc. Rev.*, 2009, **38**, 109–114.
180 J. G. McAlpin, Y. Surendranath, M. Dinca, T. A. Stich, S. A. Stoian, W. H. Casey, D. G. Nocera and R. D. Britt, *J. Am. Chem. Soc.*, 2010, **132**, 6882–6883.
181 M. W. Kanan, J. Yano, Y. Surendranath, M. Dinca, V. K. Yachandra and D. G. Nocera, *J. Am. Chem. Soc.*, 2010, **132**, 13692–13701.
182 D. Friebel, M. Bajdich, B. S. Yeo, M. W. Louie, D. J. Miller, H. Sanchez-Casalongue, F. Mbuga, T. C. Weng, D. Nordlund, D. Sokaras, R. Alonso-Mori, A. T. Bell and A. Nilsson, *Phys. Chem. Chem. Phys.*, 2013, **15**, 17460–17467.
183 H. S. Ahn and A. J. Bard, *J. Am. Chem. Soc.*, 2015, **137**, 612–615.
184 H. S. Ahn and A. J. Bard, *Anal. Chem.*, 2015, **87**, 12276–12280.
185 J. G. McAlpin, T. A. Stich, C. A. Ohlin, Y. Surendranath, D. G. Nocera, W. H. Casey and R. D. Britt, *J. Am. Chem. Soc.*, 2011, **133**, 15444–15452.
186 D. K. Bediako, Y. Surendranath and D. G. Nocera, *J. Am. Chem. Soc.*, 2013, **135**, 3662–3674.
187 S. Koroidov, M. F. Anderlund, S. Styring, A. Thapper and J. Messinger, *Energy Environ. Sci.*, 2015, **8**, 2492–2503.
188 M. Risch, F. Ringleb, M. Kohlhoff, P. Bogdanoff, P. Chernev, I. Zaharieva and H. Dau, *Energy Environ. Sci.*, 2015, **8**, 661–674.
189 D. K. Bediako, C. Costentin, E. C. Jones, D. G. Nocera and J. M. Saveant, *J. Am. Chem. Soc.*, 2013, **135**, 10492–10502.
190 H. Liu, R. More, R. Mueller, T. Fox and G. R. Patzke, *ACS Catal.*, 2015, **5**, 3791–3800.
191 J. Chivot, L. Mendoza, C. Mansour, T. Pauporte and M. Cassir, *Corros. Sci.*, 2008, **50**, 62–69.
192 B. S. Yeo and A. T. Bell, *J. Am. Chem. Soc.*, 2011, **133**, 5587–5593.
193 R. Subbaraman, D. Tripkovic, K. C. Chang, D. Strmcnik, A. P. Paulikas, P. Hirunsit, M. Chan, J. Greeley, D. Stamenkovic and N. M. Markovic, *Nat. Mater.*, 2012, **11**, 550–557.
194 M. Garcia-Mota, M. Bajdich, V. Viswanathan, A. Vojvodic, A. T. Bell and J. K. Norskov, *J. Phys. Chem. C*, 2012, **116**, 21077–21082.
195 M. Bajdich, M. Garcia-Mota, A. Vojvodic, J. K. Norskov and A. T. Bell, *J. Am. Chem. Soc.*, 2013, **135**, 13521–13530.
196 Y. Aoki, H. Habazaki, S. Nagata, A. Nakao, T. Kunitake and S. Yamaguchi, *J. Am. Chem. Soc.*, 2011, **133**, 3471–3479.
197 C. W. Moore, J. Li and P. A. Kohl, *J. Electrochem. Soc.*, 2005, **152**, A1606–A1612.
198 W. B. Davis, W. A. Svec, M. A. Ratner and M. R. Wasielewski, *Nature*, 1998, **396**, 60–63.
199 M. M. Waegele, H. Q. Doan and T. Cuk, *J. Phys. Chem. C*, 2014, **118**, 3426–3432.
200 E. Edri and H. Frei, *J. Phys. Chem. C*, 2015, **119**, 28326–28334.
201 H. S. Soo, A. Agiral, A. Bachmeier and H. Frei, *J. Am. Chem. Soc.*, 2012, **134**, 17104–17116.
202 E. Galoppini, W. Guo, W. Zhang, P. G. Hoertz, P. Qu and G. J. Meyer, *J. Am. Chem. Soc.*, 2002, **124**, 7801–7811.
203 W. Stoeber, A. Fink and E. Bohn, *J. Colloid Interface Sci.*, 1968, **26**, 62–69.
204 H. D. Sikes, J. F. Smalley, S. P. Dudek, A. R. Cook, M. D. Newton, C. E. D. Chidsey and S. W. Feldberg, *Science*, 2001, **291**, 1519–1523.
205 W. B. Davis, M. A. Ratner and M. R. Wasielewski, *Chem. Phys.*, 2002, **281**(2–3), 333–346.
206 R. L. Lemke and C. R. Lorenz, *Recent Res. Dev. Electroanal. Chem.*, 1999, **1**, 73–89.